

# Chapter 1

## The COMPASS Experiment at CERN

The COmmon Muon Proton Apparatus for Structure and Spectroscopy (COMPASS) experiment is a fixed target experiment located in France in the North Area at CERN. COMPASS started taking data in 2002 in the same hall as earlier European Muon Collaboration (EMC), New Muon Collaboration (NMC) and Spin Muon Collaboration (SMC) experiments. COMPASS has studied hadron structure through (SI)DIS, Drell-Yan and Primakoff reactions and has done hadron spectroscopy measurements.

CERN is the European Organization for Nuclear physics research. It is located part in France and part in Switzerland and includes many experiments and accelerators providing beam to these experiments. The accelerator beam lines are connected and feed beam to each other resulting in an increase in beam momentum at each successive accelerator. A schematic of the accelerators at CERN is shown in Fig. 1.1 where the accelerator that sends beam to COMPASS is the Super Proton Synchrotron (SPS).

The COMPASS spectrometer is a two-stage spectrometer. The two stages are series where each stage contains various tracking detectors and a muon wall filter at the end of each stage. Any particles that penetrate through the active area of either of the muon wall filters are with a high probability, muons. Both stages also contain an electromagnetic and hadron calorimeter. The stages are both centered around a strong spectrometer magnet used for determining particle momentum. The first stage downstream of the target is the large angle spectrometer (LAS) and it is centered around the SM1 magnet which has an integrated field of 1 Tm. This stage detects tracks with larger polar scattering angles roughly between 26 mrad and 160 mrad. The second stage is the small angle spectrometer (SAS) and it detects particle tracks having a scattering angle between roughly 8 mrad and 45 mrad. This stage is centered around the SM2 magnetic which has an integrated field of 4.4 Tm.

The left and right side of the spectrometer are referred to by the mountains that surround the spectrometer. When looking down the beam line the left side is referred to as the Jura side which roughly corresponds to the west side and the right side is referred to as the Saleve side which roughly corresponds to the east side. A graphic of the 2015 setup is shown in Fig 1.2.

This chapter gives an overview of the general COMPASS data taking setup and highlights the specific

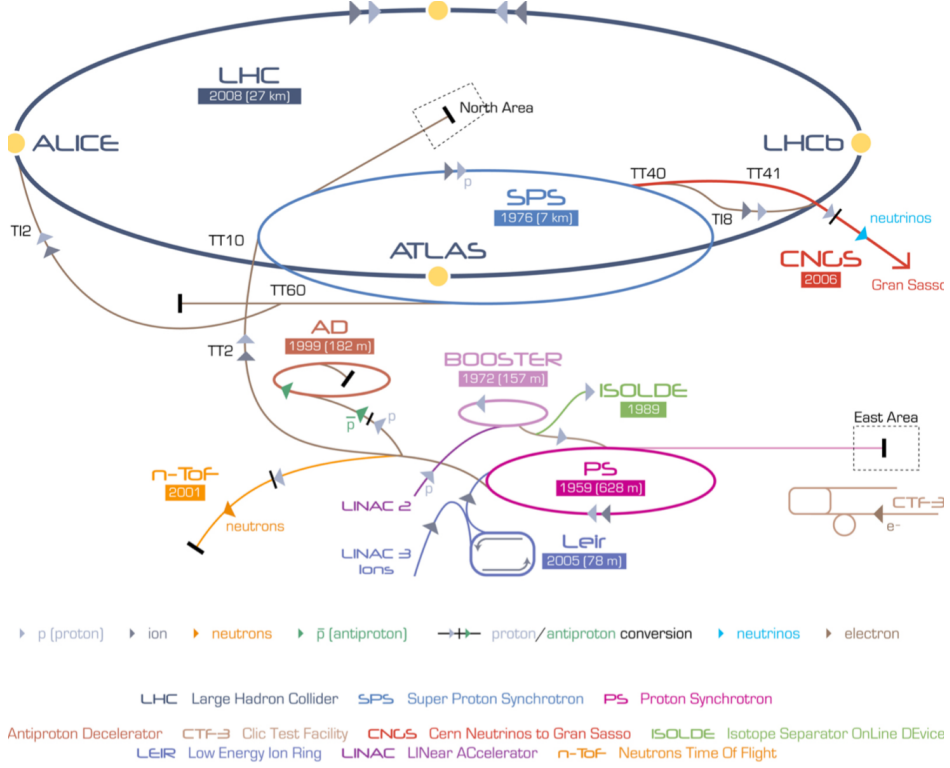


Figure 1.1: The CERN experiments and accelerators

features in 2015. All the data in this thesis was produced with the 2015 setup. For a more thorough review of the spectrometer see reference [1]. This chapter is roughly organized by how the data taking occurs and concludes with an extra section summarizing the unique features of the 2015 Drell-Yan data taking conditions.

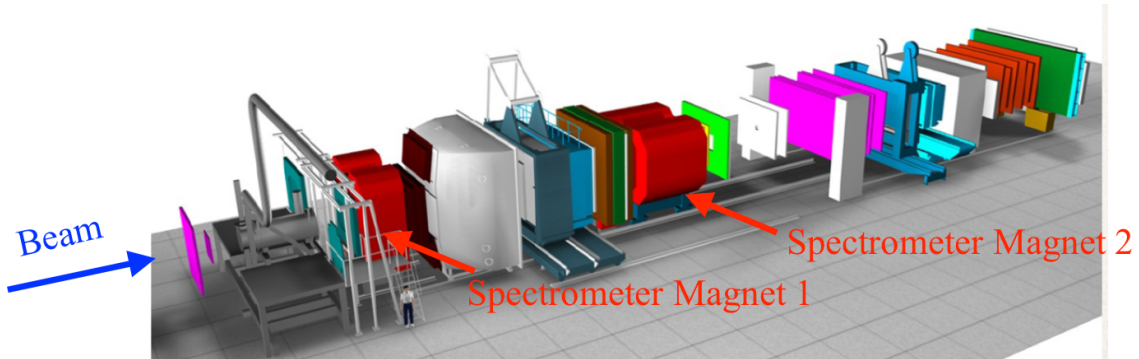


Figure 1.2: A schematic of the 2015 COMPASS setup

## 1.1 The Beam

The COMPASS spectrometer receives beam from the Super Proton Synchrotron along the M2 beam line. A schematic of the components in the M2 beam line is shown in Fig. 1.3. The SPS is the second largest accelerator at CERN with a circumference of almost 7 km which accelerates protons up to an energy of 450 GeV. The SPS extracts beam to famous Large Hadron Collier and as well sends beam to various experiments in the North Area at CERN. While the COMPASS spectrometer is above ground, the SPS is below ground and the M2 beam line must bend the beam from below ground to ground level.

There are several different beam types and energies available to COMPASS. The beam types used for physics analysis are a tertiary muon beam up to 190 GeV/ $c$  and secondary hadron beam with an energy up to 280 GeV/ $c$ . Both of the previous beam types can have a positive or negative charge. As well as the other two beam types it is also possible to have a low intensity tertiary electron beam, mainly used for calibrations.

The start of the M2 beam line is the T6 target. The SPS can accelerates primary protons up to 400 GeV/ $c$  to impinge on this T6 target which produces a secondary beam. The nominal proton intensity on the T6 target is  $100 \times 10^{11}$  spill $^{-1}$ . The T6 target is made of beryllium and has an adjustable length. The longer the T6 target the higher the secondary intensity where 500mm is the longest and typical target length used for physics data taking. The reaction of the proton beam with the T6 mainly produces secondary protons, pions and kaons. Following this reaction a series of dipole and quadruple magnets select the momentum and charge of interest.

The SPS spill structure varies throughout the data taking year depending mainly on the needs of the Large Hadron Colider (LHC). In 2015 the average intensity provided was  $0.6 \times 10^8$  s $^{-1}$  and the typical spill structure was two 4.8 second spills every 36 seconds.

### 1.1.1 Muon Beam

The muon beam is a tertiary beam which results from a weak decay of the secondary beam. After the initial proton reaction on T6 the resulting secondary particles are momentum and charge selected and sent through a 600m tunnel with focusing and de-focusing (FODO) quadruple magnets. In this tunnel the secondary pions and kaons can decay as

$$\pi^{-(+)} \rightarrow \mu^{-(+)} + \bar{\nu}_{\mu^-}(\nu_{\mu^+}) \quad (1.1)$$

and

$$K^{-(+)} \rightarrow \mu^{-(+)} + \bar{\nu}_{\mu^-}(\nu_{\mu^+}), \quad (1.2)$$

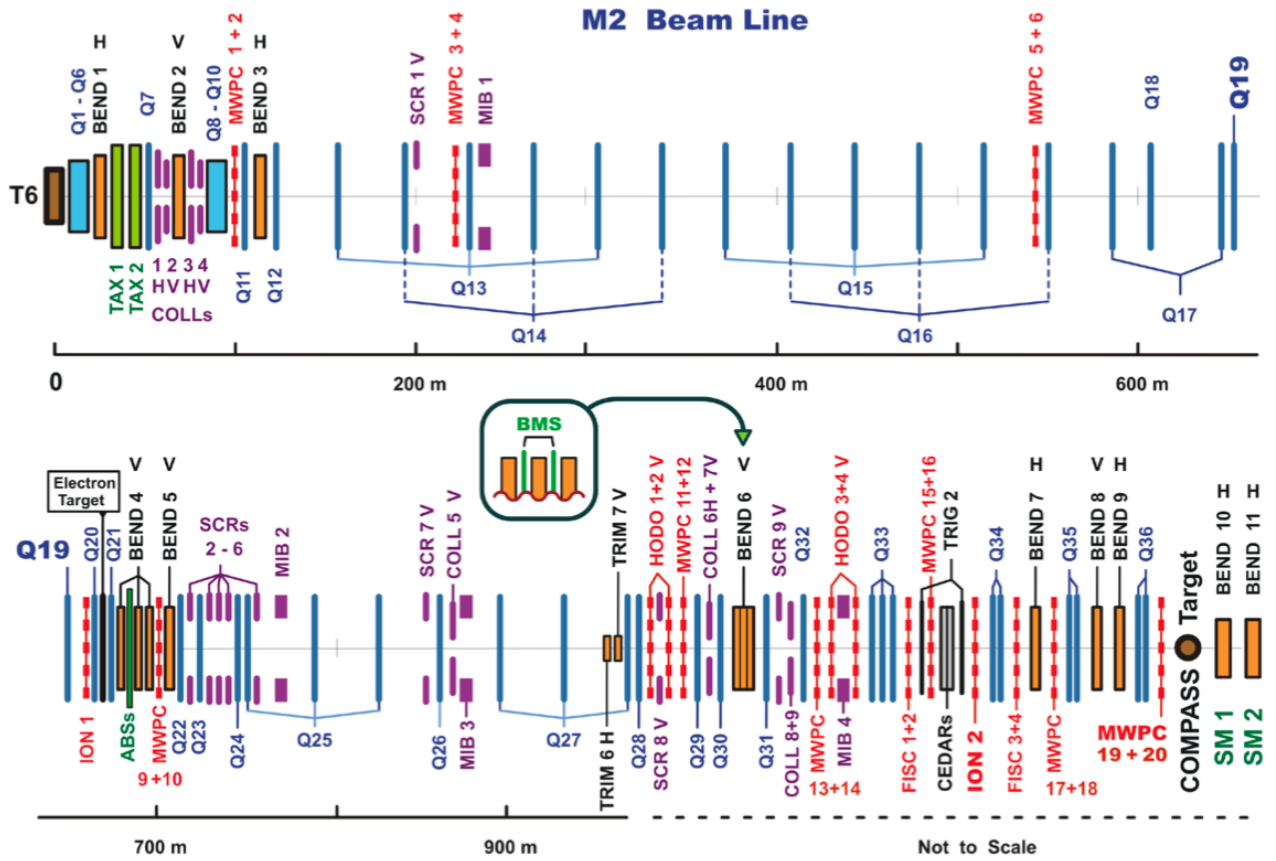


Figure 1.3: The M2 beam line at CERN

where  $K^{-(+)}$  is a kaon of negative or positive charge. At the end of the tunnel, a series of nine 1.1 m long beryllium absorbers, referred to as the ABS in Fig. 1.3, remove the remaining hadron component which did not decay. A 172 GeV/c secondary pion beam is chosen to achieve a 160 GeV/c tertiary muon beam. Due to the fact that the neutrino in the reactions 1.1 and 1.2 is always left handed, the muon will naturally be longitudinally polarized. For the muon momentum chosen, the muon beam achieves a polarization of 80%.

### 1.1.2 Hadron Beam

To deliver a hadron beam to COMPASS the ABS absorbers are not used. The decayed muons used for the tertiary muon beam have a lower momentum than the hadron beam and are therefore removable by magnetically rejecting these lower momentum muons. In the case of a negative hadron beam as in 2015, the composition of the beam is approximately 97 %  $\pi^-$ , 2.5% kaons and 0.5%  $\bar{p}$ . The 2015 Drell-Yan data taking was performed with a 190 GeV/ $c$  hadron beam.

### 1.1.3 Additional Beam Line Components

After the decay tunnel the beam is bent upwards along another FODO tunnel. The length of this tunnel is 250m and reaches the surface level approximately 100m before the COMPASS target. A series of three dipole magnets, called bend 6, then bend the beam to a horizontal position aimed at the COMPASS target. Both upstream and downstream of bend 6, there are three tracking detectors (BM01-BM06) that make up the Beam Momentum Station (BMS). The BMS is the upstream most component of the COMPASS spectrometer. It is able to determine the beam momentum to better than 1% of the beam momentum with an efficiency of approximately 93%. Bend 6 and the BMS are shown schematically in Fig. 1.4.

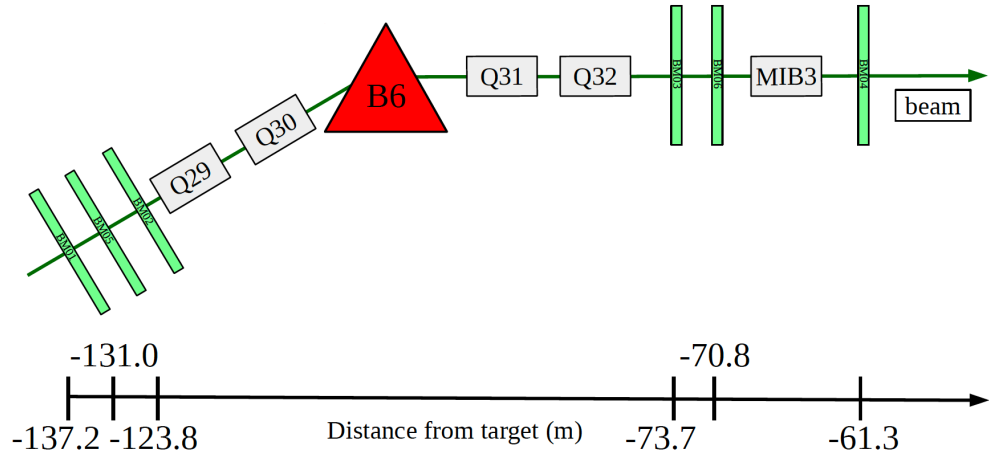


Figure 1.4: Bending the beam to a horizontal position. The BMS detectors are upstream and downstream of the bend 6 magnet.

During the 2015 Drell-Yan setup the  $\pi^-$  beam intensity was too high for the BMS station to work properly. For this reason, special low intensity, approximately  $10^6 \text{ s}^{-1}$ ,  $\pi^-$  beams were used in 2014 to determine the momentum distribution during Drell-Yan data taking. The beam momentum distribution is shown in Fig. 1.5 where the average momentum is 190.9 GeV/ $c$  with a spread of  $\pm 3.2 \text{ GeV}/c$ .

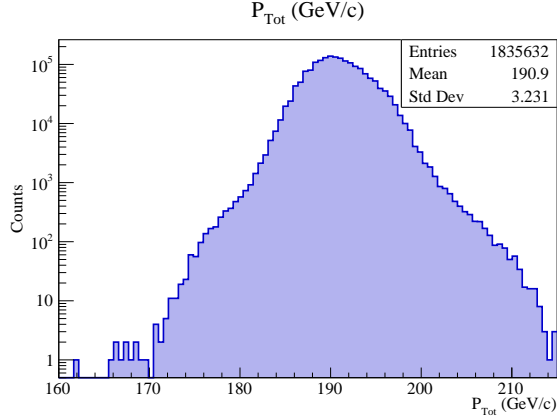


Figure 1.5: The momentum distribution of the  $\pi^-$  beam, determined during dedicated low intensity beam conditions

Approximately 30 m upstream of the target are two Cherenkov counter (CEDAR) detectors. As the hadron beam has contamination from several components these CEDARs can be used to distinguish between the different components. The CEDARs at COMPASS are high pressure detectors and have been demonstrated to achieve fast particle identification for particle momentums up to 300  $\text{GeV}/c$ . The CEDARs general principle of operation is that two particles with the same momentum but different mass will emit Cherenkov radiation at different angles relative to their momentum. When a particle is traveling faster than the speed of light in a given medium, it emits Cherenkov radiation in a cone centered along its momentum axis. The faster the particle is traveling the narrower the angle of the Cherenkov light cone. A schematic of the CEDAR operating principle is shown in Fig. 1.6. In 2015 the CEDARs were measured to be largely inefficient due to the high beam intensity and are not used for the analysis of this thesis.

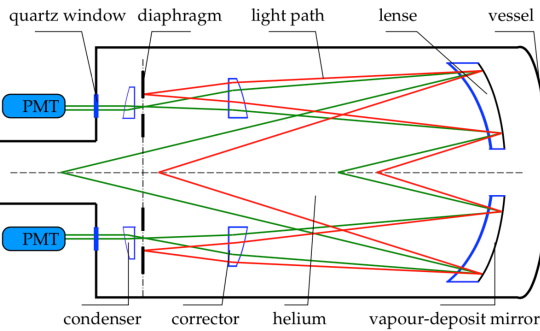


Figure 1.6: Light lines emitted inside CEDARs at COMPASS. The red(green) lines correspond to Cherenkov light emitted from a particle.

For years with a transversely polarized target, such as 2015, a chicane system of dipole magnets is setup in front of the target. The chicane first bends the beam away from the beam line and then back to the

target such that the beam hits the target at an angle. A chicane magnet setup is used because a beam hitting the target without any angle would then be deflected from the target magnet to the left or right of the spectrometer. For this reason the chicane gives the beam an angle before hitting the target such that the non-interacting beam exits the target traveling straight towards the spectrometer.

## 1.2 The Polarized Target

The polarized target at COMPASS is the most complicated and essential component of the spectrometer. It is located upstream of the tracking detectors and spectrometer magnets and downstream of the beam telescope, described in section 1.3, detectors. The target consists of two or three cylindrical cells. The possible materials are either solid state ammonia ( $\text{NH}_3$ ) or deuterated lithium ( ${}^6\text{LiD}$ ) or liquid hydrogen. Fig. 1.7 shows a schematic of the target.

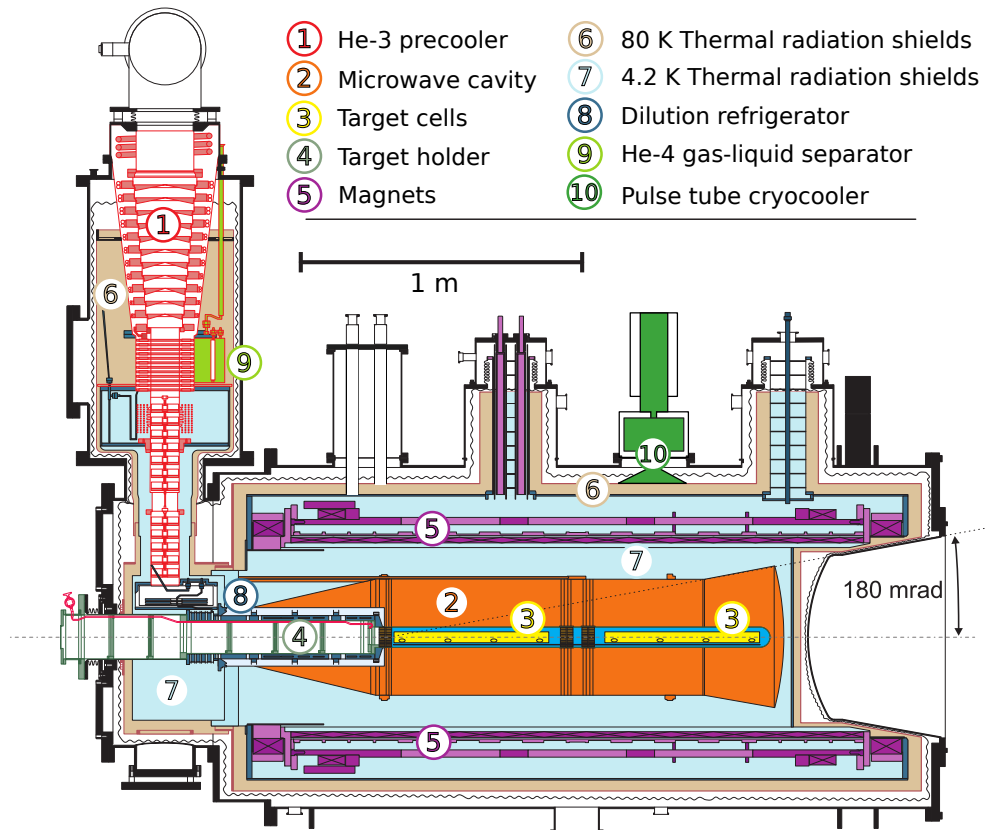


Figure 1.7: The polarized target at COMPASS

Surrounding the cylindrical cells is a longitudinal super conducting magnet capable of reaching a magnetic field of 2.5 T. This longitudinal magnet polarizes the target parallel or anti-parallel to the direction of the

beam momentum. The target polarization is maintained by keeping the target in a liquid helium bath of approximately 60 mK. This is called frozen spin mode where the temperature is maintained by a dilution refrigerator.

The target is polarized through the dynamic nuclear polarization (DNP) method [2]. This process works by first polarizing electrons in the target with the longitudinal magnet. With a high probability, the target electrons are all polarized in the same longitudinal direction for each target cells. Due to their much lower mass, electrons have a larger magnetic moment and therefore can be polarized at a much faster rate than protons or neutrons. At the same time the electrons are being longitudinally polarized, microwave electromagnetic radiation is sent through each target cell. For atoms which have a nuclear spin it is then possible for these atoms to absorb a microwave going to an excited state with the electron spin anti-parallel to the magnet and the nuclear spin either parallel or anti-parallel to the magnet depending on the microwave frequency. To ensure only one frequency enters each target cell, there is a microwave stopped between each target cell. The electron with the anti-aligned spin will then quickly have its spin realigned while the nucleon will take much longer to lose its polarization due to its smaller magnetic moment. This process can continue in this way resulting in a net nuclear polarization. Using the DNP method the target can achieve a polarization of approximately 90% in three days.

The target also includes a 0.63T transverse dipole magnet to change from longitudinal polarization to transversely polarized. The target must first be longitudinally polarized before the transverse target magnet can change the polarization direction. Once the target is transversely polarized, the target polarization can no longer be increased as microwaves can no longer shine on the target in the polarization direction. Therefore the polarization will decrease exponentially. In 2015 the target was polarized for about half a day between data taking sub-periods ad achieved an average polarization of 0.73%, including the effects of exponential polarization lose with time. The target transverse polarization relaxation time was about 1000 hours in 2015.

The target polarization was measured with 10 NMR coils while the target cells were longitudinal polarized. In the 2015, each target cell had the most upstream and downstream coils in the center of the target cell and the other three coils on the outside perimeter as is shown in Fig. 1.8. Due to the fact that the polarization can only be measured with the longitudinal magnet on, the polarization is only measure at the start and finish of a transversely polarized data taking. The intermediate polarization is then determined by exponential interpolating between these two times.

In 2015 the setup was two transversely polarized target cells of 55 cm length and 2 cm in radius. The cells were separated by 20 cm and polarized in opposite directions. The polarization of the target cells was flipped

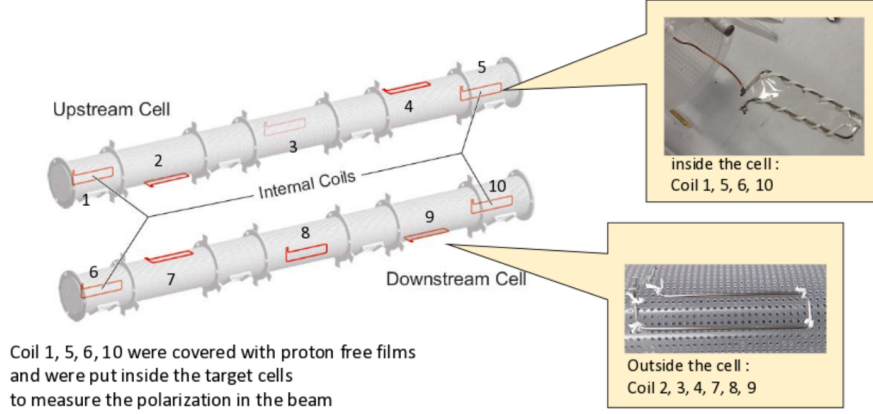


Figure 1.8: The empty polarized target cells side by side along with their NMR coil positions

ever two weeks of data taking to reduce systematic effects from luminosity and geometrical spectrometer acceptance. Due to the fact that the beam needs to be precisely steered onto the target and that the chicane magnets upstream of the target are setup for only one transverse target magnet direction, the transverse target magnet only pointed downward in 2015. To achieve a polarization flip the target polarization had to therefore be rotated back to the longitudinal direction and the input microwaves had to be changed to achieve the desired polarization direction.

The target material in 2015 was solid state NH<sub>3</sub>. The protons in the three hydrogen atoms were the only nucleons with nuclear spin and therefore only some fraction of the target was able to be polarized. The fraction of polarized nucleons to total nucleons is called the dilution factor. Counting the ratio of unpolarized nitrogen nucleons to polarized hydrogen, one would expect the dilution to be 3/17. However to get a more accurate determination of the dilution factor the follow calculation was used

$$f = \frac{n_H \sigma_{\pi^- H}^{DY}}{n_h \sigma_{\pi^- H}^{DY} + \sum_A n_A \sigma_{\pi^- A}^{DY}}, \quad (1.3)$$

where  $f$  is the dilution factor,  $n_H$  is the number of hydrogen atoms in NH<sub>3</sub>,  $n_A$  is the number of other nucleons in NH<sub>3</sub>, and  $\sigma_{\pi^- H}^{DY}$  and  $\sigma_{\pi^- A}^{DY}$  are the Drell-Yan cross-section for pion hydrogen scattering and

pion nucleon scattering respectively. The cross-sections were determined using a parton-level Monte-Carlo program MCFM [3]. The dilution factor was also further scaled down by studies of reconstruction migration between target cells. The average dilution factor in 2015 was determined to 0.18 in the invariant mass range of  $4.3(\text{GeV}/c)^2$  to  $8.5(\text{GeV}/c)^2$ .

## 1.3 Tracking Detectors

To determine when and where a reaction occurs in the polarized target, tracking detectors are able to position the products the reaction. The goal of the tracking detectors is to determine a point in space where a particle traversed. The COMPASS tracking detectors attempt to do this for a wide range of angles, momentums and at different rates. For these reasons there are several planar tracking technologies used at COMPASS which can be divided into three categories: very small angle tracker, small angle trackers and large area trackers. As the name suggest very small angle trackers measure tracks with small angle deflections from the beam axis which are essentially beam particles. The small area trackers measure particle tracks with low but non-zero scattering polar angle and have small central dead zones. The large area trackers are several meters in height and width and measures the largest deflection angles up to 180 mrad.

All of these trackers are split into stations. Each station corresponds to several detectors planes at roughly the same z-position along the beam line. Each station measures a track position in one or more orientation while most measure tracks in three or more orientations. The coordinate orientations measured are the X and Y coordinates which are the horizontal and vertical directions respectfully, and as well the U and V coordinates which are rotated at different angles with respect the X and Y coordinates.

### 1.3.1 Very Small Angle Trackers

The very small angle trackers extend up to 3 cm away from the beam axis. This is the region with the highest number of tracking particles and therefore these detectors must be able to handle the highest rates up to  $5 \times 10^7$  Hz. The two detector types that make up the very small angle trackers are either scintillating fiber detectors (SciFi) or silicon microstrip detectors. These two detector types are complementary to each other as the former have very good timing resolution while the latter have very good spacial resolution.

There are three silicon stations possible at COMPASS. These stations have active detecting areas of  $5 \times 7 \text{ cm}^2$ . The spacial resolution of these detectors is nominally  $10 \mu\text{m}$  and the timing resolution is nominally 2.5 ns. For the 2015 setup, the beam intensity was too high for the silicon detectors to operate and therefore these detectors were not used.

There are 10 SciFi stations available at COMPASS. The active areas vary from  $3.9 \times 3.9 \text{ cm}^2$  to  $12.3 \times 12.3 \text{ cm}^2$  planar areas. As well the detection fiber diameters vary between detectors with the different diameters used at COMPASS being 0.5 nm, 0.75 nm and 1 nm. Several fibers are bundled together to determine a strip hit position and the resulting nominal spacial resolutions are  $130 \mu\text{m}$ ,  $170 \mu\text{m}$  and  $210 \mu\text{m}$ . The nominal timing resolution of these detectors is about 400 ps. In 2015 three SciFi stations made up the beam telescope and were placed upstream of the target to measure the beam trajectory and timing information. A fourth SciFi station was place in the LAS section of the spectrometer.

### 1.3.2 Small Angle Trackers

The small angle trackers detect particles with non-zero deflection angles. These detectors have medium size active areas compared to the very small angle trackers and the large angle trackers. They cover 5 cm to 40 cm from the beam axis where the rate drops to approximate  $10^5 \text{ Hz}$ , two orders of magnitude lower than the rates the very small angle trackers receive. At COMPASS there are two types of small area tracking detectors: micromesh gaseous structure (micromegas) and gas electron multipliers (GEMs).

There are three micromega stations at COMPASS. All three stations are location sequentially after each other between the target and the first spectrometer magnet. As well all three detectors measure four coordinate projections and have an active area of  $40 \times 40 \text{ cm}^2$  with a 5 cm diameter dead zone. The micromegas operate by having a conversion region and a smaller amplification region. An ionized particle produced in the conversion region will drift through an electric field of around  $3.2 \text{ kV/cm}$  to the amplification region where the electric field is around  $50 \text{ kV/cm}$ . The electric field is too small for amplification in the conversion region but as the name suggest the electric field is high enough to amplify the signal in the amplification region. The amplified signal is then read out on strips. The conversion and amplification regions are separated by a metallic micromesh material. The electrons pass through the micromesh without resistance and are not rimmed out. The micromegas have good spacial resolution because the thickness of the amplification region is only  $100 \mu\text{m}$ , small enough to prevent much transverse spreading of the electron avalanche between strips. The separation of the larger conversion region from the smaller amplification region with the micromesh prevents electric field lines from being distorted in the conversion region and therefore prevents the primary electrons from drifting slower in the conversion region. This allows micromegas to operate at a higher rate than would be possible otherwise. This principle of operation is illustrated in Fig. 1.9. The strips in the central part of the detector are  $360 \mu\text{m}$  corresponding to a resolution of about  $100 \mu\text{m}$  and the strips in the outer region are  $460 \mu\text{m}$  corresponding to a resolution of about  $120 \mu\text{m}$ . The nominal timing resolution 9 ns. In 2015 the micromegas were upgraded to include a pixelized section covering much of the dead zone area.

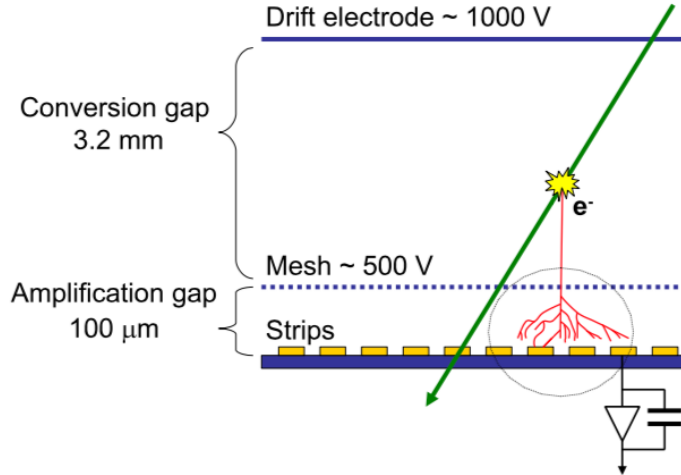


Figure 1.9: Principle of operation for the micromesh gaseous structures (micromegas)

There are eleven GEM detectors located throughout the COMPASS spectrometer. The first GEMs are located after the first spectrometer magnet and the last GEMs are located near the end of the spectrometer. These detectors are positioned close to the beam axis. They are mounted on a large area tracker, covering the dead zone region of the large area tracker. All eleven detectors have an active area of  $31 \times 31 \text{ cm}^2$  and a 5 cm diameter dead zone. In times of lower beam intensity the dead zones can be turned on as an active area.

The detector is split into four regions. These regions are separated by a polyimide foil (50  $\mu\text{m}$  thick) having around  $10^4 \text{ cm}^{-1}$  drifting holes of 70  $\mu\text{m}$  diameter and are clad with copper on both sides. There is an electric potential of a few hundred volts between each foil layer. The electron amplification occurs around the holes of each of the three foil dividers. This means GEM detectors speed up the amplification process by splitting the amplification avalanche into three locations. The process is sped up because the drifting electrons are accelerated multiple times thereby speeding up their drifting velocity which therefore reduces the overall drift time from the ionization location to the strip readout. This allows the GEMs to operate at a higher rate than would otherwise be possible. The principle of operation is illustrated in Fig. 1.10. The nominal timing and spacial resolution of the GEM detectors is 10 ns and 110  $\mu\text{m}$  respectively. Two pixelized GEM detectors were also in operation but were not as crucial for the 2015 Drell-Yan measurement.

### 1.3.3 Large Area Trackers

The large area trackers measure the largest polar scattering angles at COMPASS. Their dead zones mostly coincide with a small area tracker, described in the previous section 1.3.2, which therefore means these

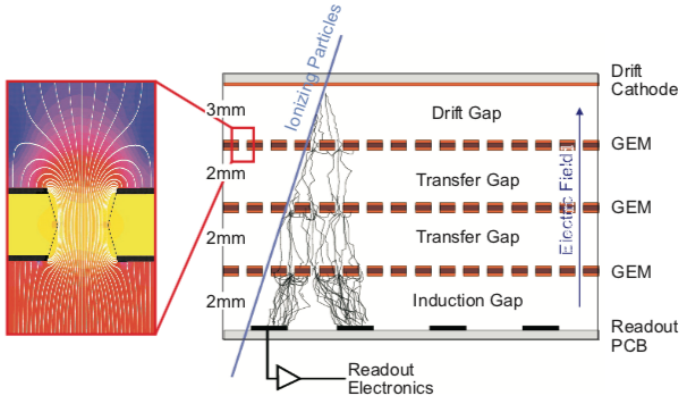


Figure 1.10: The operation principle of the gas electron multiplier (GEM) detectors

detectors do not have to process the higher fluxes very close to the beam line. The most important feature of these detectors is that they have a large planar area. As a consequence however, their position and timing resolutions are not as good as the small and very small angle trackers. The types of large area trackers used at COMPASS are all gaseous detectors and include drift chambers (DCs), straw tube detectors (straws) and multi-wire proportional chambers (MWPCs).

The first four drift chambers downstream of the target are named DC00, DC01, DC04 and DC05. The first two, DC00 and DC01, have smaller active areas of  $180 \times 127 \text{ cm}^2$  and a circular dead zone of 30 cm diameter. These two drift chambers are positioned upstream of the SM1 magnet. The rates upstream of SM1 are higher. This is due to the fact that low energy particles are produced in the target, but are bent out of the acceptance of spectrometer by SM1. Therefore detectors downstream of SM1 do not track these low energy particles and therefore DC00 and DC01 need to be able to process a higher particle flux. The next two drift chambers, DC04 and DC05, are downstream of SM1 and both have larger active areas of  $240 \times 204 \text{ cm}^2$  and as well have dead zones of 30 cm diameter. The active areas of all four of these DCs was roughly chosen to coincide with the acceptance of the SM1 yoke. DC05 was first installed for the 2015 Drell-Yan data taking and is further described in chapter ???. All four of these DCs measure four projection views corresponding to eight detector layers. A sketch of the principle of operation is shown in Fig. 1.11. The nominal spacial resolution for these detectors is  $250 \mu\text{m}$ .

Further downstream the spectrometer, downstream of the SM2 magnet, are the W45 drift chamber stations. The W45 drift chambers are the largest drift chambers at COMPASS. There are six W45 detector stations which each have an active area of  $520 \times 260 \text{ cm}^2$  and a circular dead zone of 50 cm or 100 cm diameter.

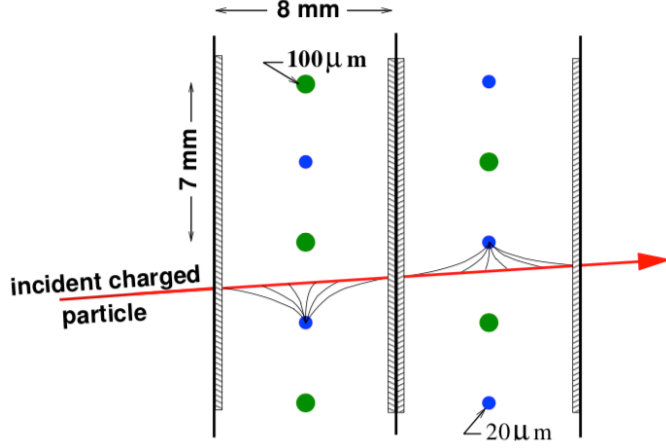


Figure 1.11: Drift cell of a drift chamber with the ionized drift electron lines coming from the incident charged particle

Each W45 station measures two projection views corresponding to four detector layers. The drift cells in W45 are  $40 \times 10 \text{ mm}^2$  and the spacial resolution is nominally  $1500 \mu\text{m}$ .

The two straw stations in operation during the 2015 data taking are named ST03 and ST05. ST03 was in the large angle spectrometer after DC05 and consisted of two stations measuring six projection views. ST05 was in the small angle spectrometer and measured three projection views. The active areas of each of the horizontal wire stations is  $350 \times 243 \text{ cm}^2$  and the active area of each of the rotated wires is  $323 \times 272 \text{ cm}^2$ . The principle of operation for the straw detectors is very similar to that of a drift chamber. However, instead of having the detector made up of connected drift cells the straw detectors are made of separated circular tubes. Each tube consist of a gold plated tungsten anode wire in the center and the walls of the tube make up a cathode. Due to the fact that the cathode completely surrounds the anode wire there is no electrical interference between neighboring anode wires as there is for drift chambers. For this reason the electric field in each tube is easier to control and the ionized electron drift speed is more linear than other detectors. Each straw detector plane is divided into sections where the straw tubes in the outer most section from the beam line have a diameter of 9.6 mm and the tubes close to the beam line have a diameter of 6.1 mm. In addition, in the central part of the detector there is a physical hole, dead zone of  $20 \times 20 \text{ cm}^2$ . The nominal position resolution for these detectors is  $400 \mu\text{m}$ . A frontal schematic is shown in Fig. 1.12. For the reason that most of the detected muons are reconstructed in the large angle spectrometer and the fact that many of the high voltage modules were not operation for ST05 in 2015, ST05 was not used for track reconstruction for 2015 Drell-Yan data.

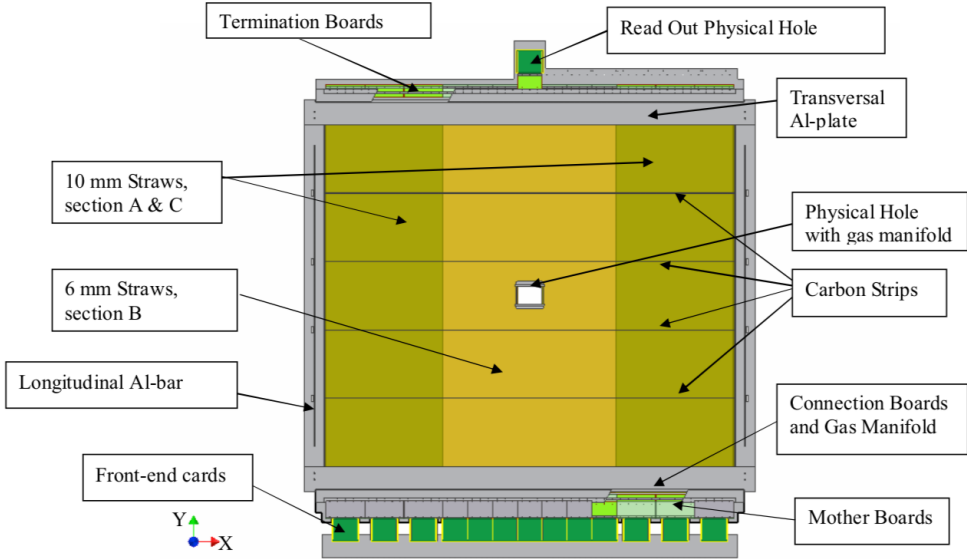


Figure 1.12: Front on view of a the active area of a straw detector at COMPASS

The next type of large angle track is the richwall. This large area tracker operates similarly to the straw tube detectors. The detector consist of eight layers of mini drift tubes (MDT) shown in Fig. 1.13. The central part of each MDT includes a gold plated tungsten sense wire. The richwall is located before the SM2 magnet and after ST03 with an active area of  $5.27 \times 3.91 \text{ cm}^2$  and a central dead zone of  $1.02 \times 0.51 \text{ cm}^2$ . The nominal position resolution of this detector is  $600 \mu\text{m}$ .

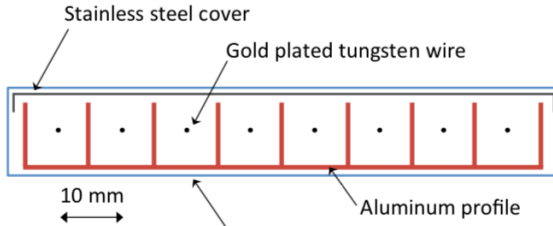


Figure 1.13: The richwall mini drift tubes

The final type of large area tracking detector at COMPASS is the MWPC. There are 14 of these stations located throughout the experiment. The MWPCs are separated into three categories distinguished by the coordinates they measure. The first type is called type A and consists of three projection views measuring an x, u and v coordinate. The second type is type A\* and is the same as type A but measures the y coordinate in addition to the other three coordinates. Both type A and A\* have active areas of  $178 \times 120 \text{ cm}^2$ . The final type is type B which has a smaller active area of  $178 \times 90 \text{ cm}^2$  and measures the same projections as type A.

There are seven stations of type A, one station of type A\* and six stations of type B. All three types have circular dead zones of diameters 16 cm, 20 cm and 22 cm for types A, A\* and B respectively.

The MWPCs operate on similar principles to the drift chambers but without a calibration drift curve. For this reason the MWPCs can be made to have one common gas volume between each station. Their position resolution is determined as

$$\frac{\text{sense wire separation}}{\sqrt{12}}, \quad (1.4)$$

which is the variance of a uniform distribution. The separation between sense wires is approximately 2 mm which corresponds to a spacial resolution of these detectors of around 600  $\mu\text{m}$ .

## 1.4 Particle Identification

In the COMPASS spectrometer there are four types of detectors used to determine particle identification (PID). These four detectors are the ring image Cherenkov (RICH) detector, electromagnet calorimeters (ECAL), hadron calorimeters (HCAL) and muon walls (MW). The RICH distinguishes between pions, kaons and protons; ECAL1 and ECAL2 measure the energy from photons and electrons; HCAL1 and HCAL2 measure the energy from hadrons; and MW1 and MW2 distinguish muons from all other particles. The RICH, ECAL1, HCAL1 and MW1 are in the large angle spectrometer in that respective order along the beam line. The small angle spectrometer includes ECAL2, HCAL2 and MW2 again in that respective order along the beam line.

The RICH detector operates similarly to the CEDARS, section 1.1.3. In the RICH, Cherenkov radiation is emitted from particles traveling through it at an angle dependent on the particle's velocity. The RICH is filled with a dielectric gas,  $\text{C}_4\text{F}_{10}$ , which has an index of refraction greater than air. The momentum of a particle going through the RICH is determined from bending radius around SM1. Therefore once the RICH determines the entering particle's velocity, the mass of particles can be distinguished. A sketch of the RICH and its operating principle is shown in Fig. 1.14. To distinguish between particles the minimum momenta are: 2.5  $\text{GeV}/c$  for pions, 9  $\text{GeV}/c$  for kaons and 17  $\text{GeV}/c$  for protons. The maximum momentum the RICH can distinguish between any of these particles is 50  $\text{GeV}/c$ . This detector is located in the large angle spectrometer before any calorimeters.

The ECALs and HCALs both measure the energy of entering particles. Both types of calorimeters do this by stopping a specific entering particle, where the amount of energy deposited in each respective calorimeter is proportional to the incoming particle's energy. ECALs are able to stop and measure electron and ph-

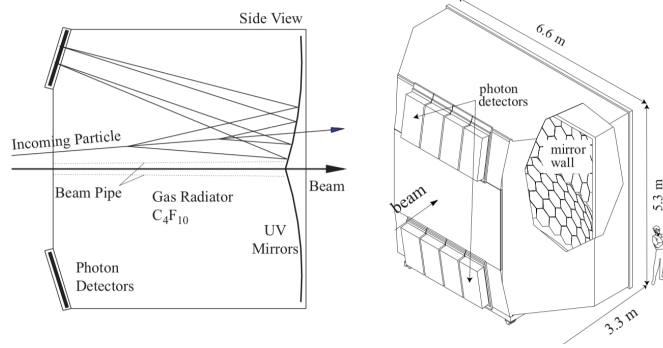


Figure 1.14: Side view demonstrating the principle of operation of the RICH detector.

ton energies and HCALs stop and measure hadron energies. The energy knowledge along the momentum determined from the tracking detectors allows the ability to determine the particle's identification.

The ECALs are made of lead glass towers with photon multipliers attached to these towers on one side. An incoming photon or electron interacts with the lead glass to produce a light signal which is readout with these photon multipliers. Other particles also interact with the material in the ECALs however hadrons and muons are able to exit through the detector unlike photons and electrons. A frontal view of ECAL1 is shown in Fig. 1.15 and a frontal view of ECAL2 is shown in figure Fig. 1.16.

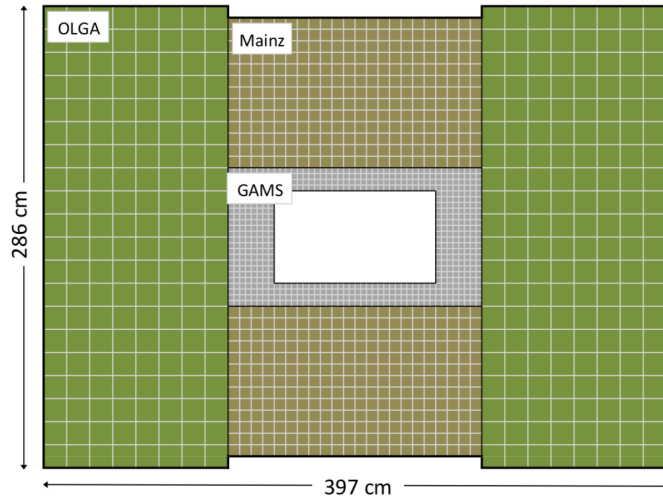


Figure 1.15: Frontal view of the electromagnetic calorimeter 1

The HCALs are sampling calorimeters which are made of alternating layers of iron and scintillating material. An incoming hadron deposits all its energy in the HCAL by making a particle showers in the iron. This particle shower makes a signal in the scintillating material which is then read out by photo multipliers. The HCALs are placed after the ECALs in each stage of the spectrometer because an electromagnetic shower happens within less material budget than a hadronic shower. The HCALs are effect at determining particle

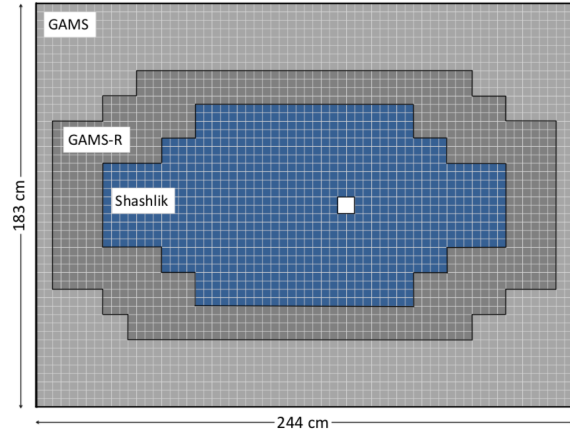


Figure 1.16: Frontal view of the electromagnetic calorimeter 2

energies from particle with energies between 10 GeV and 100 GeV.

The two MWs are located after an HCAL in their respective stages. Due to their higher mass and absence of color charge, muons are able to pass through the most material budget of any of the particles detected at COMPASS. For this reason both MWs consist of an absorber and tracking detectors downstream of this absorber. Any particles that make it through the absorber are with a very high probability muons.

MW1 consists of eight tracking planes before a 60 cm iron absorber and the same number of tracking planes after this absorber. The tracking portions of MW1 are built similarly to the richwall, described in section 1.3.2, in that they are also made of MDT modules. The active area of MW1 is  $480 \times 410 \text{ cm}^2$  and includes a dead zone of  $140 \times 80 \text{ cm}^2$ . Each plane of this detector has a spacial resolution of 3 mm. A sketch of MW1 is shown in Fig. 1.17.

The second muon wall, MW2, is located downstream of a 2.4 m thick concrete absorber. MW2 consists of 12 planes each with an active area of  $450 \times 450 \text{ cm}^2$  and a dead zone of  $90 \times 70 \text{ cm}^2$ . The detector operates similarly to the straw detectors, section 1.3.2, in that the detector is made of drift tubes with a wire in the center of these tubes. The diameter of the drift tubes is 29 mm and the position resolution is about 1.4 mm.

There is one last absorber in the COMPASS spectrometer located before the H5 hodoscope at the end of the spectrometer hall. This absorber is called muon filter 3 (MW3) and ensures that the inner trigger is only triggered by a muon.

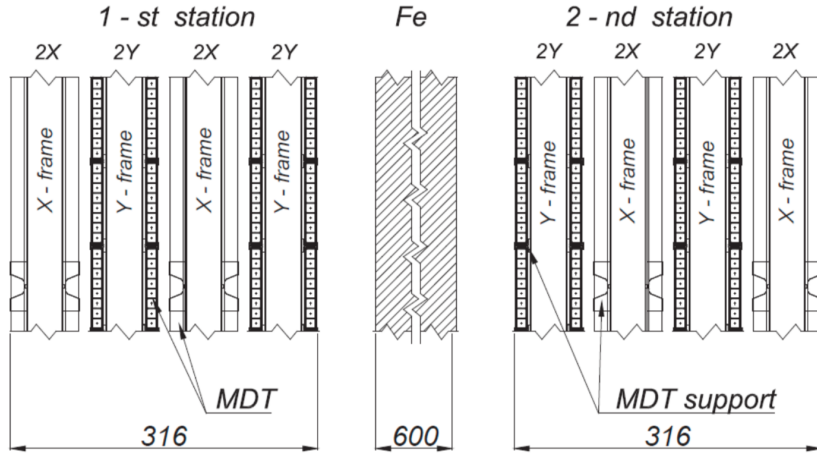


Figure 1.17: A side view sketch of the muon wall 1 detector

## 1.5 Trigger

The trigger system at COMPASS defines what is an event. Whenever the trigger signal is given, all the detector information within a few nanosecond timing window is recorded. Due to the fact that there are very many background events occurring as the beam impinges on the target, there is too much information going to the front end modules (FEMs) of the detectors for the FEMs to process and record all this information. For this reason only a certain subset of all the information is stored to disk. The trigger system must therefore have good timing resolution to make quick decisions on which data to record. At COMPASS the trigger systems consist of scintillating hodoscopes attached to PMTs. The timing resolution of these detectors is approximately 1 ns. A top view schematic of COMPASS showing where the relative positions of the hodoscopes for each trigger is shown in Fig. 1.18.

At COMPASS there are five different triggers used to register physics events. Each trigger type includes at least two hodoscopes at different z-positions in the spectrometer. The types of triggers are either target pointing, when the hodoscope slabs are horizontal; or energy loss, when the hodoscope slabs are vertical. The target pointing trigger is setup and used with higher polar scattering angles. As the name suggest, this trigger signals when a particle is scattered from the target. The energy loss trigger is used to trigger on lower  $Q^2$  interactions and signals when a particle is bent a specified amount. This concept is illustrated in Fig. 1.19.

There are four triggers in SAS: the inner trigger (IT), the middle trigger (MT), the ladder trigger (LT) and the outer trigger (OT). The IT is an energy loss trigger and includes the hodoscopes HI04X and HI05X. The MT includes both energy loss and target pointing slabs. The hodoscopes in the MT are HM04X,

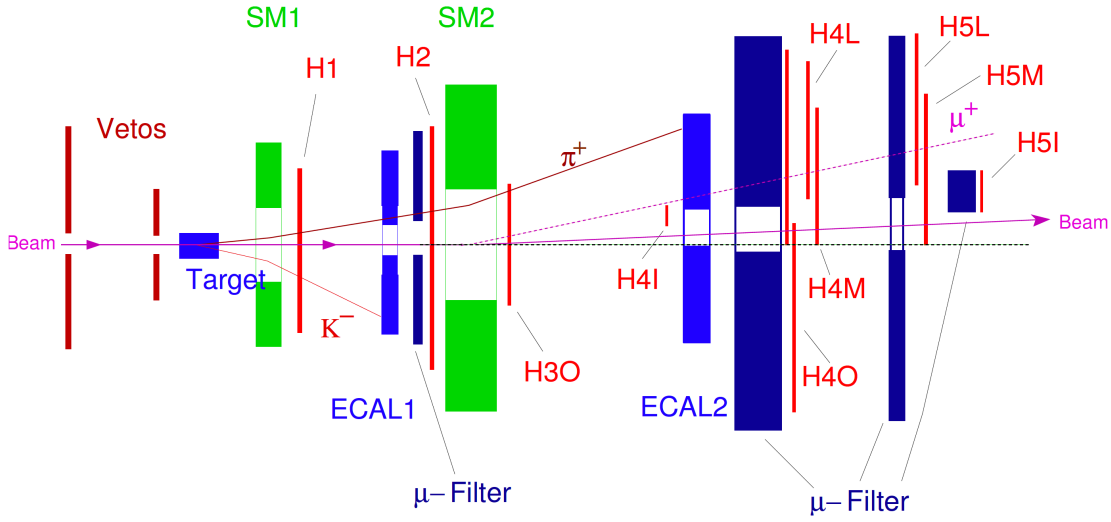


Figure 1.18: Top view of the spectrometer highlighting how different particles can signal a trigger

HM05X, HM04Y and HM05Y. The MT hodoscopes whose names end with an X have vertical slabs and those ending with a Y have horizontal slabs. The LT is an energy loss trigger which consists of HL04X and HL05X. The final trigger in SAS, the OT, is a target pointing trigger and consists of hodoscopes HO03Y and HO04Y. The remaining trigger system is in LAS and is a target pointing trigger consisting of hodoscopes HG01Y and HG02Y. The kinematic coverage for the 2015 triggers is shown in Fig. 1.20.

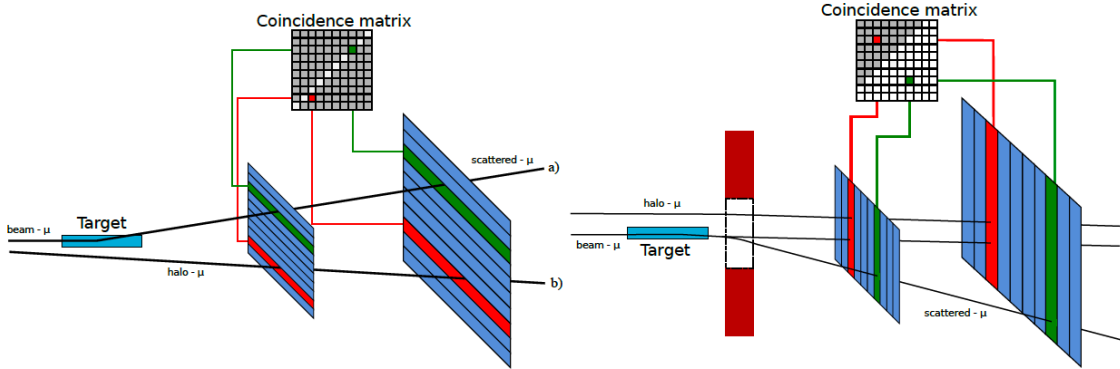


Figure 1.19: The two types of triggers (left is target pointing and right is energy loss) at COMPASS and an illustration of the coincidence matrix used to select events of interest

In addition to signaling when interesting events occur, it is also important to signal when background events are occurring. For this reason there is also a veto system upstream of the target as shown in Fig. 1.18. This veto trigger consists of hodoscopes attached to PMTs as well. It is centered on the beam axis but has a hole in the center on the nominal beam line. The veto trigger is used to reject halo muons which surround the beam.

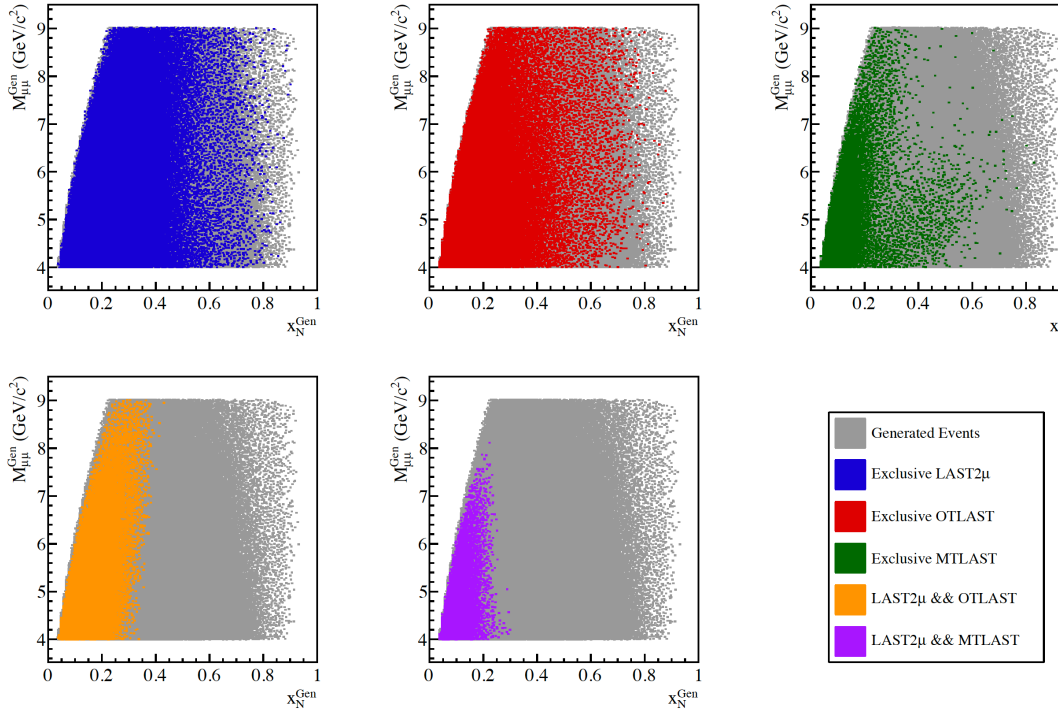


Figure 1.20: The kinematic coverage for the 2015 triggers determined from Monte-Carlo studies

Halo muons result from the beam decaying, as in Eq. 1.1 and Eq. 1.2, where this decay occurs upstream of the target but downstream of the ABS absorbers. The muon halo surrounds the hadron beam due to the muon's lower momentum, and it is for this reason that the veto hodoscopes, outside of the beam line, are able to reject events that would occur due to the halo.

There is one trigger in the spectrometer hall that is not a hodoscopes. This is the calorimeter trigger (CT). The CT can be used as a trigger when a particle deposits more than a certain energy threshold in the specified calorimeter. In 2015 this trigger was only used as an independent study of the other triggers at COMPASS. Particularly the CT was used to measure the trigger hodoscopes efficiencies.

The last trigger used at COMPASS is a random trigger. This trigger is setup outside of the spectrometer area and registers a signal when a radioactive source disintegrates. In this way the random trigger is truly random. In 2015 this trigger was used in studies of the beam flux.

In 2015, the goal was to measure two muons in the spectrometer. For this reason, two triggers must each signal a particle in coincidence for an event to be registered. For physics analysis the coincidence triggers are either two muons in LAS (LASxLAS), one muon in LAS and one in the OT (LASxOT) or one muon in LAS and one muon in the MT (LASxMT). The LASxLAS trigger system covers the high  $Q^2$  and high  $x_{\text{beam}}$  phase space whereas the triggers including a SAS hodoscope cover lower  $Q^2$  values. In addition to

these three dimuon triggers where three single muon triggers corresponding to a particle in LAS, MT or OT. These three single muon triggers, however, were pre-scaled down to only take every 500, 100 or 100 events respectively. For further tests 2015 included a random trigger and a beam trigger pre-scaled down by 35000.

## 1.6 Data Acquisition

The data acquisition (DAQ) collects data from the over 250,000 detector channels and transfers this data to storage on magnetic tape at CASTOR (CERN Advanced STORage). Despite the triggering system used to reduce the data rate, the data still is recorded at event rates between 10 kHz to 100 kHz. A typical COMPASS event size is 45 kB. The DAQ is designed to process these data rates and size while minimizing the dead time associated with data collection and transfer. In 2015 the dead time was approximately 10%. The total data the DAQ recorded, after the spectrometer finished commissioning, was approximately 750 terabytes of raw data.

Data collection begins with the digitization of information from a detector channel. This digitization is performed by a time to digital converter (TDC) or an analogue to digital converter (ADC). These TDCs and ADCs are either on the detector FEMs or on custom COMPASS readout electronics named: GANDOLF (Generic Advanced Numerical Device for Analog and Logic Functions), GeSiCA (Gem and Silicon Control and Acquisition) or CATCH (COMPASS Accumulate Transfer and Control Hardware). After digitization the data is transferred by optical fibers to an FPGA multiplexer where the data is buffered by spill and arranged by event. From there an FPGA switch sends the data to multiplexer slaves. The slaves are online computers that oversee the final steps for raw data and transfer this data to CASTOR. This whole process is shown schematically in Fig. 1.21.

## 1.7 Data Reconstruction

The COMPASS Reconstruction and AnaLysis Program (CORAL) reconstructs the raw data into physical quantities. For example CORAL is able to convert the raw data into particle tracks with momentum, charged and possibly an originating vertex location [4]. The raw data from the DAQ is digitized timing information from tracking detectors or digitized energy information for calorimeters. The process of reconstructing tracks takes the detector timing information and determines a position in space for a particular tracking detector based on a calibration. CORAL then uses a Kalman Filter to determine straight tracks in regions with no or low magnetic field [5]. The tracks are then connected through the magnetic field using a fast lookup table for known possible bending radii. At this point a track is determined to have a momentum, charge and a  $\chi^2$

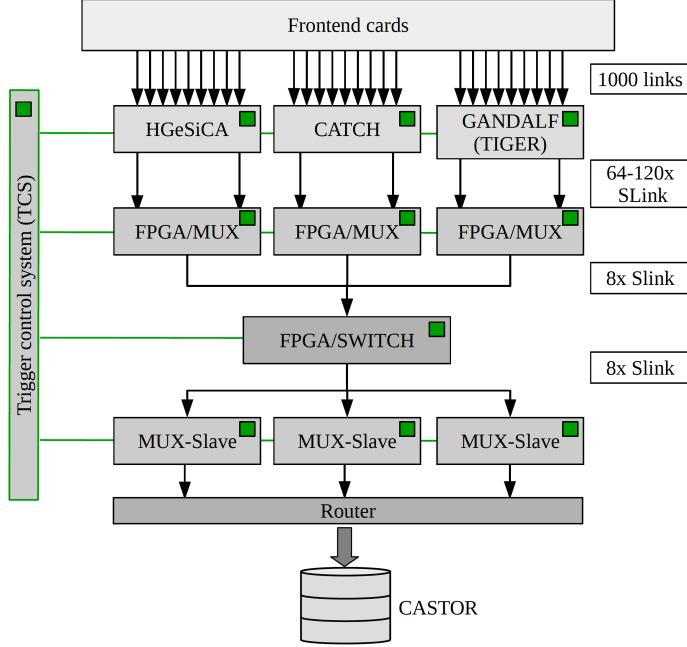


Figure 1.21: The data acquisition steps at COMPASS

value associated with the track. From there the tracks are extrapolated back to the target region and the intersection of at least two tracks is determined as a vertex. If in addition to the two intersecting tracks, a beam particle can be extrapolated forward to the same vertex location then the vertex is assigned to be a primary vertex. Otherwise the vertex is defined as a secondary vertex.

This reconstruction stage reduces the data volume by approximately a factor of 10. A diagram of the reconstruction data flow is shown in Fig. 1.22. In 2015 there were several data reconstructions performed. Between each reconstruction improvements were made to detector calibrations, detector alignment, beam tracking and any other preprocessing improvements that could be made. The final two productions are the t3 production and the slot1 production. The results shown in this thesis are from either t3 or slot1 productions.

Once reconstruction has been performed the data is stored in data structured trees (DSTs). The usual procedure of reconstruction which gives physical values such as momentum and charge to tracks, results in data called miniDSTs. There is also the possibility to save more information, for example detector hit location information, to make so called fatDSTs. These DSTs are now in a format which can be processed by PHAST (PHysics Analysis Software Tool). PHAST is a COMPASS program written to further analyze physics data. With PHAST there is the possibility to loop over all the miniDSTs and make certain cuts and to produce a so called  $\mu$ DSTs based on these cuts. In 2015  $\mu$ DSTs were made for all the analysis data where a cut was applied to the miniDSTs saving only events with at least two muons. Both CORAL and

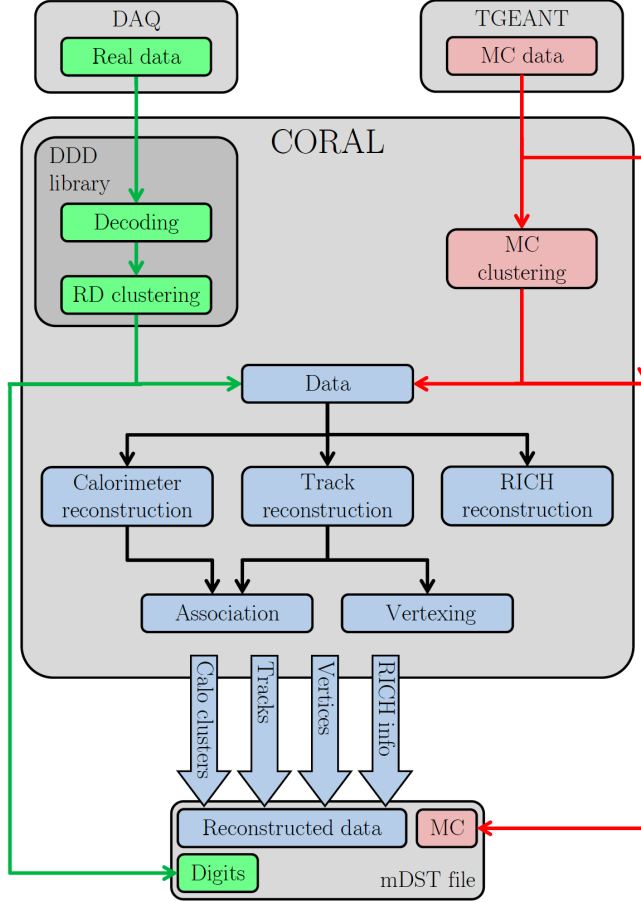


Figure 1.22: The schematic of the CORAL reconstruction process

PHAST are fully object-oriented C++ programs.

### 1.7.1 Monte-Carlo Production

Monte-Carlo data is simulated data which is performed in three steps. First a programs generates specific physics processes based on their theoretical probabilities. The generators of Monte-Carlo used for this thesis are PYTHIA versions 6 and 8 [6]. Next a GEANT4 simulation of COMPASS determines if a detector will register a hit from these generated physics processes. This saves the data in a raw data format which can be reconstructed by CORAL. Finally the simulated data is reconstructed by CORAL and analyzed in PHAST the same as if the data were real data.

## 1.8 2015 Drell-Yan Data Taking

The 2015 Drell-Yan data taking is one of the main programs for the COMPASS-II experiment. The data taking began in April of 2015 and ended in November of that year. The physics data used for analysis started in July and finished at the end of data taking. The data recorded before July was used for calibrations and commissioning. The total analysis data was split into nine data periods labeled W07-W15 where each data period corresponded to approximately two weeks of beam time. The spin orientation of each target cell was reversed after the first week of every period to reduce systematic effects arising from different geometric acceptances and luminosities of the up and downstream target cells.

### 1.8.1 Hadron Absorber

The previous sections in this chapter described the spectrometer setup generally and mentioned the specifics for the 2015 setup. The main unique hardware addition in 2015 is the hadron absorber. The hadron absorber was installed because the beam intensity is high and results in many main strong interactions in the target. For this reason the first tracking detectors upstream of SM1 have occupancies which are too high for tracking. Therefore the hadron absorber was installed to prevent all particles except muons from entering the spectrometer.

The hadron absorber was placed just downstream of the two target cells as can be seen in Fig. 1.23. The absorber corresponded to approximately 7.5 interactions lengths of material where the material was mostly alumina ( $\text{Al}_2\text{O}_3$ ) and concrete. Inside the absorber was an aluminum target followed by a tungsten plug, each of radius 2.5 cm. The tungsten was used as a beam dump while the aluminum was present to prevent back scattering from the tungsten beam plug. A side view showing the dimensions and materials used can be seen in Fig. 1.24. Both the aluminum target and tungsten plug served the double purposes as absorbers and also as unpolarized nuclear targets. In addition to the hadron absorber two thin  ${}^6\text{Li}$  absorbers were added just downstream of the primary absorber to absorb thermal neutrons produced in the primary absorber. This  ${}^6\text{Li}$  absorber was proposed to improve the performance of the first tracking detector downstream of the target even with the hadron absorber installed.

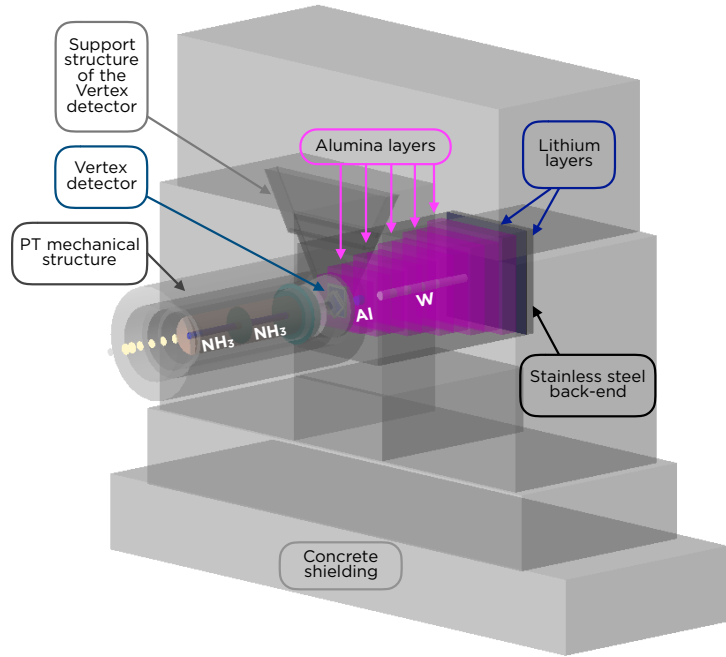


Figure 1.23: The hadron absorber downstream of the polarized target in 2015

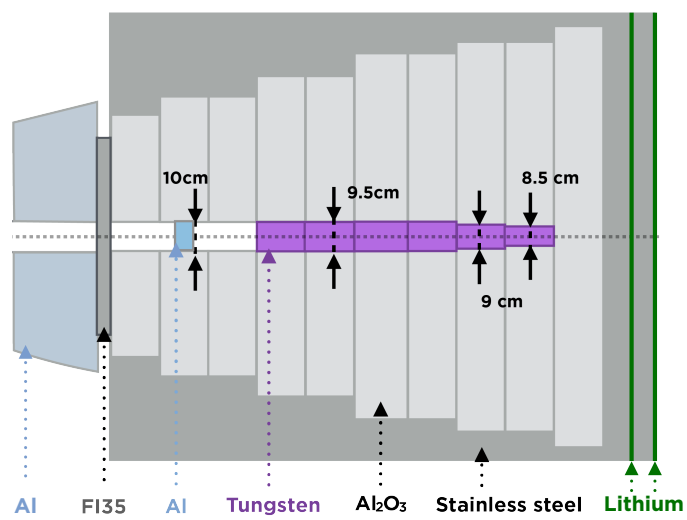


Figure 1.24: Side view of the hadron absorber used in 2015

# Chapter 2

## Analysis of High Mass Drell-Yan Transverse Spin Phenomena

This chapter goes over the analysis techniques and results from the 2015 transversely polarized Drell-Yan data taking. The chapter begins by describing the data collection setup and the event selection criteria followed by the analysis techniques used to determine asymmetry amplitudes. The analysis techniques described are the standard transverse spin-dependent asymmetry (TSA) analysis, Sec 2.2, the double ratio analysis, Sec 2.3, the  $q_T$  weighted asymmetry analysis, Sec 2.4, and finally the left-right asymmetry analysis, Sec 2.5. All of these analyses are related in that they measure TMD effects from the Drell-Yan process. For this reason the event selection and kinematical asymmetry binning described in the opening sections will be the same for all analyses in this chapter unless stated otherwise.

### 2.1 Data Sample

#### 2.1.1 Data Collection

The data sample is from the 2015 COMPASS Drell-Yan measurement where a 190 GeV/c  $\pi^-$  beam impinged on a transversely polarized NH<sub>3</sub> target. The COMPASS spectrometer began taking commissioning data in April of 2015. The data collected for this analysis, after the commissioning phase, is from July 8 through November 12. The data is split into 9 periods lasting approximated 2 weeks each. During each data period the spectrometer conditions were frozen so no detector changes could effect the spectrometer acceptance. Each period is split into two sub-periods. To reduce systematic effects of acceptance and luminosity dependencies, the NH<sub>3</sub> target was split into two oppositely polarized cells with one cell polarized vertically up and one cell polarized vertically down in the lab frame. The cells were separated by 20 cm and the polarization of both cells was flipped between sub-periods. A summary of the analysis data taking from each period is shown in Table 2.1.

Period	Sub-period	Polarization	First-Last run	Begin date	End date
W07	one	$\downarrow\uparrow$	259363 - 259677	July 9	July 15
	two	$\uparrow\downarrow$	259744 - 260016	July 16	July 22
W08	one	$\uparrow\downarrow$	260074 - 260264	July 23	July 29
	two	$\downarrow\uparrow$	260317 - 260565	July 29	August 5
W09	one	$\downarrow\uparrow$	260627 - 260852	August 5	August 12
	two	$\uparrow\downarrow$	260895 - 261496	August 12	August 26
W10	one	$\uparrow\downarrow$	261515 - 261761	August 26	September 1
	two	$\downarrow\uparrow$	261970 - 262221	September 4	September 9
W11	one	$\downarrow\uparrow$	262370 - 262772	September 11	September 22
	two	$\uparrow\downarrow$	262831 - 263090	September 23	September 30
W12	one	$\uparrow\downarrow$	263143 - 263347	September 30	October 7
	two	$\downarrow\uparrow$	263386 - 263603	October 8	October 14
W13	one	$\downarrow\uparrow$	263655 - 263853	October 15	October 21
	two	$\uparrow\downarrow$	263926 - 264134	October 22	October 28
W14	one	$\uparrow\downarrow$	264170 - 264330	October 28	November 2
	two	$\downarrow\uparrow$	264429 - 264562	November 4	November 8
W15	one	$\downarrow\uparrow$	264619 - 264672	November 9	November 11
	two	$\uparrow\downarrow$	264736 - 264857	November 12	November 16

Table 2.1: COMPASS 2015 data taking periods

### 2.1.2 Stability Tests

To ensure the data analyzed were recorded during stable beam and spectrometer conditions, stability of the analysis data was performed on a spill-by-spill and run-by-run basis. The data was recorded in runs with a maximum of 200 spills per run and where one spill can have several thousand events.

#### Bad Spill Analysis

To determine if a given spill is deemed unstable several macro variables were averaged over the spill and compared to neighboring spills. These macro variables were chosen specifically to be sensitive to the general stability conditions of the spectrometer and are listed in the follower enumerated list Table 2.1.2. The starting criteria for an event was two oppositely charged muons where a muon was defined as having crossed 15 radiation lengths of material.

1. number of beam particles divided by the number of events
2. number of beam particles divided by the number of primary vertices
3. number of hits per beam track divided by the number of beam particles
4. number of primary vertices divided by the number of events
5. number of outgoing tracks divided by the number of events

6. number of outgoing particles from a primary vertex divided by the number of primary vertices
7. number of outgoing particle from primary vertex divided by the number of events
8. number of outgoing particles from primary vertex divided by the number of events
9. number of hits from outgoing particles divided by the number outgoing particles
10. number of  $\mu^+$  tracks divided by the number of events
11. number of  $\mu^+$  tracks from primary vertex divided by the number of events
12. number of  $\mu^-$  tracks divided by the number of events
13. number of  $\mu^-$  tracks from primary vertex divided by the number of events
14.  $\sum \chi^2$  of outgoing particles divided by the number of outgoing particles
15.  $\sum \chi^2$  of all vertices divided by the number of all vertices in an event
16. Trigger rates (LASxLAS, OTxLAS, LASxMT)

If the spectrometer was stable during a spill the average values from the variables in Table ?? are expected to be constant from one spill to the next. To determine if a spill was recorded in unstable conditions the spill of interest is compared with its neighboring 2500 spill occurring before and after in time. If the spill of interest is a specified sigma away from any of the neighboring spills too many times, the spill of interest is marked as a bad spill. If a spill fails this bad spill criteria for any of the macro variables in Table ?? the spill is deemed bad and not included in the analysis. The criteria for the sigma distance and number times a spill crosses this distance to be deemed a bad are different for each data taking period. In addition to checking the nearest spills for each spill, all the spills in a run are marked bad if the run it has less than 10 spills or greater than 70% bad spills. Table ?? describes the impact of the bad spill analysis on each period.

### **Bad Run Analysis**

The stability of the spectrometer is also verified on run-by-run check in parallel to the spill-by-spill check. The run-by-run analysis compares kinematic distributions and the average of these distributions per run to the same kinematic distributions and averages from the other runs in a given period. The kinematic distributions tested are:  $x_N$ ,  $x_\pi$ ,  $x_F$ ,  $q_T$ ,  $M_{\mu\mu}$ ,  $P_{\mu^+}$ ,  $P_{\mu^-}$ ,  $P_\gamma$ ,  $P_{\pi^-}$ , and vertex  $x$ ,  $y$  and  $z$  positions. The quantities in the run-by-run analysis are expected to influence the asymmetries measured, however their distributions and averages are not expected to have spin-influenced effects from the limited statistics in just

a single run. An unbinned-Kolmogorov test (UKT) is performed to compare each distributions. An UKT test is made between all the runs in a given period and a run is marked bad if it is incompatible with most of the runs in a period. The comparison of mean for each distribution from each run is made with the average from a given period. If one of the kinematical variables has an average more than five standard deviations from the average within a period, the run is rejected. The results of the bad spill rejection after having already applied the bad spill rejection are shown in Table ??.

Table 2.2: Stability analysis rejection percentages

Period	Bad spill rejection	Bad spill and spill rejection
W07	11.79%	17.94%
W08	18.00%	21.19%
W09	14.76%	17.11%
W10	15.88%	17.80%
W11	22.49%	26.14%
W12	12.71%	13.79%
W13	22.32%	22.73%
W14	8.91%	10.70%
W15	3.94%	3.94%

### 2.1.3 Event Selection

The cuts in the event selection were chosen to ensure the event consisted of two oppositely charged muons, so called dimuons, resulting from a pion collision in the transversely polarized target. The event selection was initial filtered from miniDSTs to  $\mu$ DSTs using the criteria of at least two muons detected in the spectrometer. The cuts used in this analysis are described in the following enumerated list where the event selection is performed on these  $\mu$ DSTs and the events used come from the slot1 production. A summary of the number of events remaining after the last cuts is shown in Table 2.1.

1. Two oppositely charged particles from a common best primary vertex. A primary vertex is defined as any vertex with an associated beam particle. In case of multiple common primary vertices the best primary vertex was determined by CORAL tagging the vertex as best primary (PHAST method `PaVertex::IsBestPrimary()`). In the case that CORAL did not tag any of the common vertices as the best primary the vertex with the smallest spatial  $\chi^2$  value was used as the best primary vertex.
2. A dimuon trigger fired. A dimuon trigger firing means there are at least two particles in coincidence in this event. The dimuon triggers used were a coincidence between two particles in the large angle spectrometer, LAS-LAS trigger, or a particle in the large angle spectrometer and a particle in the Outer hodoscope in the small angle spectrometer, LAS-Outer trigger. The LAS-Middle trigger was

used as a veto on beam decay muons where beam decay muons result from the decay of the beam pion, kaon or anti-proton into a muon. This beam decay muon can then be in coincidence with a positive muon from another decay or strong reaction in the target. The LAS-Middle trigger was used a veto because this trigger was found to have many events resulting from a beam pion decaying to a muon.

3. Both particles are muons. A muon was defined as having crossed 30 radiation lengths of material between the particles first and last measured points. This criteria has been previously determined to be effective at distinguishing between muons and hadrons. In the data production no detectors were used from upstream of the hadron absorber so the absorber is not included in the determination of material crossed.
4. The first measured point for both particles is before 300 cm and the last measured point is after 1500 cm. This cut ensures both particles have positions upstream of the first spectrometer magnet and downstream of the first muon filter.
5. The timing of both muons is defined. This checks that the time relative to the trigger time is determined for both muons so further timing cuts can be performed.
6. Both muons are in time within 5 nanoseconds. This track time for each muon is defined relative to the trigger time as in the previous cut. This cut helps rejected uncorrelated muons.
7. The muon track's spacial reduced  $\chi^2$ s are individually less than 10. This cut ensures track quality.
8. A validation that each muon crossed the trigger it was associated as having triggered. This trigger validation cut was performed by extrapolating (PHAST Method PaTrack::Extrapolate()) each muon track back to the hodoscopes it fired and determining if the muon crossed the geometric acceptance of both hodoscopes.
9. The event does not occur in the bad spill or run list. Many tests were performed to test the basic stability of the spectrometer and beam as described in section 2.1.2. The spills placed on the bad spill list were deemed to occur during unstable data taking conditions.
10. The Drell-Yan kinematics are physical. That is  $x_\pi$  and  $x_N$  are between 0 and 1 and  $x_F$  is between -1 and 1.
11. The transverse momentum of the virtual photon,  $q_T$  is between 0.4 and 5.0 GeV/c. The lower limit ensures azimuthal angular resolution is sufficient and the upper cut is minimal and further ensures the kinematic distributions are physically possible.

12. The vertex originated within the z-positions of the transversely polarized target cells defined by the target group ( $-294.5 < Z_{\text{vertex}} < -239.3$  for the upstream target or  $-219.5 < Z_{\text{vertex}} < -164.3$  cm for the downstream target).
13. The vertex is within the radius of the polarized target measured to be 1.9 cm.

Cuts	<b>W07</b>	<b>W08</b>	<b>W09</b>	<b>W10</b>	<b>W11</b>	<b>W12</b>	<b>W13</b>	<b>W14</b>	<b>W15</b>	<b>WAll</b>	<b>% Remaining</b>
All Data	19410	19184	19654	20707	31371	23563	20561	13154	7697	175301	100.00 %
Good Spills	15947	14899	16217	16895	23041	20184	16026	11796	7422	142427	81.70 %
$0 < x_\pi x_N < 1, -1 < x_F < 1$	15932	14886	16200	16885	23022	20171	16013	11794	7414	142317	81.70 %
$0.4 < q_T < 5(\text{GeV}/c)$	14342	13385	14609	15239	20667	18101	14365	10588	6636	127932	60.75 %
Z Vertex within NH <sub>3</sub>	4256	4024	4330	4552	6369	5503	4411	3130	2028	38603	15.05 %
Vertex Radius < 1.9cm	4175	3950	4257	4474	6252	5414	4334	3078	1987	37921	12.21 %

Figure 2.1: Event selection statistics for this analysis

### 2.1.4 Binning

The asymmetries are measured in bins of  $x_N$ ,  $x_\pi$ ,  $x_F$ ,  $q_T$ , and  $M_{\mu\mu}$ . Where  $x_N$  and  $x_\pi$  the momentum fractions of the target nucleon and beam pion respectively,  $x_F = x_\pi - x_N$ ,  $q_T$  is the transverse momentum of the virtual photon and  $M_{\mu\mu}$  is the invariant mass of the di-muon. The binning was determined by requiring equal statistical population in each kinematic bin. In addition, the asymmetries are determined in an integrated bin using all the analysis data. The analyzes binning limits are summarized in Table 2.3.

Kinematics	Lowest limit	Upper limit bin 1	Upper limit bin 2	Upper limit bin 3
$x_N$	0.0	0.13	0.19	1.0
$x_\pi$	0.0	0.40	0.56	1.0
$x_F$	-1.0	0.22	0.41	1.0
$q_T (\text{GeV}/c)$	0.4	0.86	1.36	5.0
$M_{\mu\mu} (\text{GeV}/c^2)$	4.3	4.73	5.50	8.5

Table 2.3: Analysis binning limits

## 2.2 Transverse Spin-Dependent Asymmetries

This section describes the standard TSA analysis for which the results are published in reference [7]. The main motivation for this analysis was to conclude on the sign flip of the Sivers function flip between the Drell-Yan and SIDIS processes using data from the same experimental setup for both processes. The results shown are those determined by the COMPASS Drell-Yan analysis subgroup.

The kinematical distributions shown for this analysis are the same as for the remaining analyses in this chapter. This results from the fact that all the analyses in this chapter use the same event selection and cuts. The only exception to this is for the  $q_T$ -weighted analysis, Sec 2.4, which cannot cut on  $q_T$  and therefore has a different  $q_T$  distribution as is explained in Sec 2.4.1.

As was noted in the event selection 2.1.3, the data considered are in the invariant mass range [4.3–8.5 GeV/ $c^2$ ]. Fig. 2.2 shows the invariant mass range from the 2015 COMPASS data. All cuts except a cut on invariant mass are included in Fig. 2.2 and as well a fit to show the background processes is included.

The fit is determined from Monte-Carlo data and combinatorial background analysis. The Monte-Carlo data simulated all hard processes which decay to two oppositely charged muons and can be reconstructed in the COMPASS spectrometer. Combinatorial background analysis estimates the background as  $N_{combinatorial} = 2\sqrt{N_{\mu^+}\mu^-N_{\mu^-}\mu^+}$ . As can be seen in Fig. 2.2, there are two distinguishable background peaks. The lower mass peak at about 3 GeV/ $c^2$  corresponds to  $J/\Psi$  production and the higher mass peak at around 3.6 GeV/ $c^2$  corresponds to  $\Psi'$  production. All the analyses in this chapter use the mass range between 4.3 and 8.5 GeV/ $c^2$  and as Fig. 2.2 shows, the Drell-Yan process dominates in this mass range. The background percentage was estimated to be below 4% in this mass range.

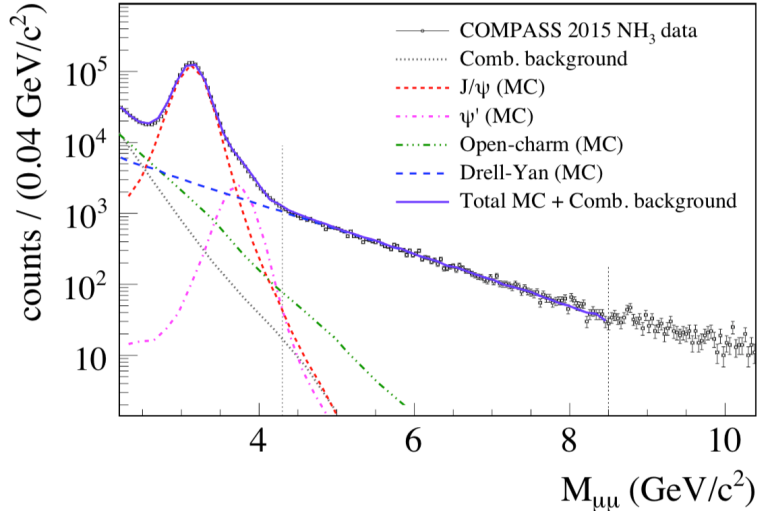
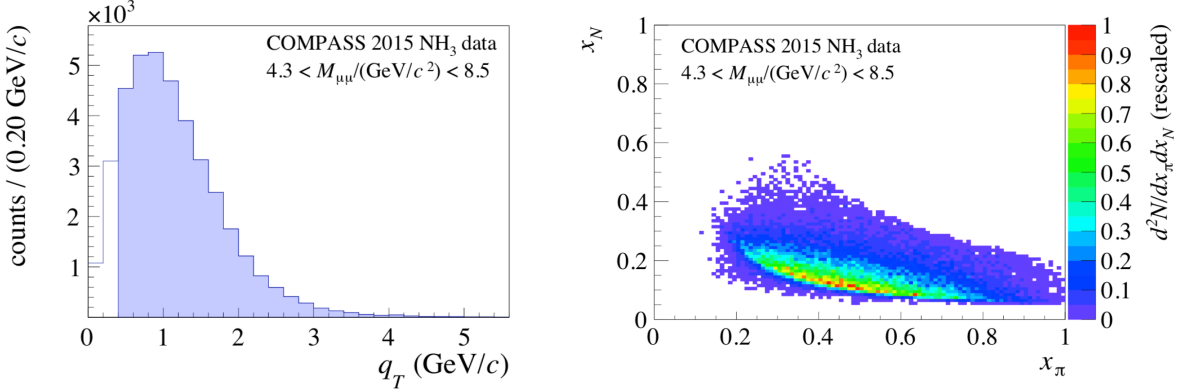


Figure 2.2: The 2015 COMPASS invariant dimuon mass distribution and a fit to this data. The data fit is from Monte-Carlo and combinatorial background analysis and is provided to show the background processes. This image is taken from [7].

Fig. 2.3a shows the transverse virtual photon momentum,  $q_T$ , distribution. With the cut on  $q_T$  between [0.4–5(GeV/ $c$ )], the average  $q_T$  is 1.2 GeV/ $c$  while on the other hand the average  $M_{\mu\mu}$  is 5.3 GeV/ $c^2$ . As stated in chapter ??, the regime where TMD functions are the theoretical model for parton distributions is when  $q_T \ll M_{\mu\mu}$ . While the average  $q_T$  is less than the average  $M_{\mu\mu}$ , it is not excluded that the results

in this chapter are outside of the TMD regime. Nevertheless all the results presented in this chapter are determined assuming the TMD description is valid.



(a) The  $q_T$  distribution where the shaded region shows the data used in the high mass analysis and the unshaded region shows the full distribution without a  $q_T$  cut. This image is taken from [7].

(b) The 2-dimensional distribution of  $x_\pi$  vs.  $x_N$ . Both  $x_\pi$  and  $x_N$  are safely in their respective valence regions. This image is taken from [7].

The distribution of  $x_\pi$  versus  $x_N$  is shown in Fig. 2.3b. The Bjorken-x of the proton,  $x_N$ , is almost exclusively above 0.1 and as well Bjorken-x for the pion,  $x_\pi$  is in its valence region. For these reasons it is safe to say that the Drell-Yan reaction studied in the following analyses is the result of the pion's anti-u-quark annihilating with the proton's u-quark.

The results from TSA analysis are determined from an extended unbinned maximum likelihood fit to the data. The dilution and depolarization values are determined on an event by event basis unlike the other analyses in this chapter. The released integrated results for the leading order and sub-leading order TSAs are shown in Fig. 2.4. The leading order TSAs are non-zero with approximate significances of: 1 sigma for the Sivers TSA,  $A_T^{\sin(\phi_S)}$ , 1.2 sigma for the Pretzelosity TSA,  $A_T^{\sin(2\phi_{CS} + \phi_S)}$  and 2 sigma for the transversity TSA,  $A_T^{\sin(2\phi_{CS} - \phi_S)}$ .

The comparison of the Sivers TSA,  $A_T^{\sin(\phi_S)}$ , with the expected sign flip is shown in Fig. 2.5. The positive solid theory curves show the expected Sivers TSA assuming the Sivers function flips sign between Drell-Yan and SIDIS. The main difference in these three theory curves is the  $Q^2$  evolution which is also the main uncertainty in each prediction. As can be seen the Sivers TSA is compatible with the expected sign change. However, the error bars on the Sivers asymmetry amplitude are too large to conclusively distinguish between the three theory curves or even to conclusively conclude on the sign change between Drell-Yan and SIDIS. That being said, the amplitude  $A_T^{\sin(\phi_S)}$  is 2 sigma away from being incompatible with a sign flip.

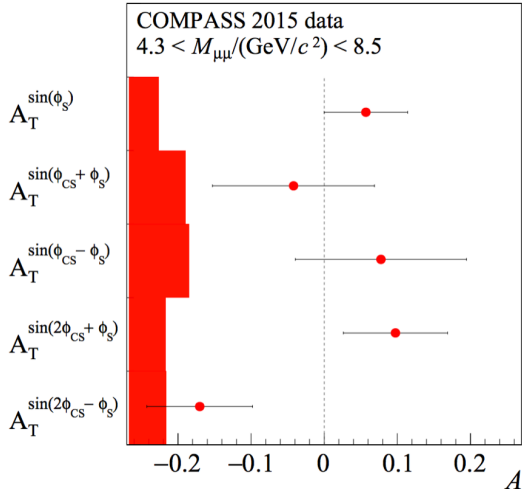


Figure 2.4: The integrated TSAs with statistical and systematic error bars.  $A_T^{\sin(\phi_s)}$ ,  $A_T^{\sin(2\phi_{CS}+\phi_s)}$ , and  $A_T^{\sin(2\phi_{CS}-\phi_s)}$  are leading order TSAs and  $A_T^{\sin(\phi_{CS}+\phi_s)}$  and  $A_T^{\sin(\phi_{CS}-\phi_s)}$  are sub-leading order TSAs.

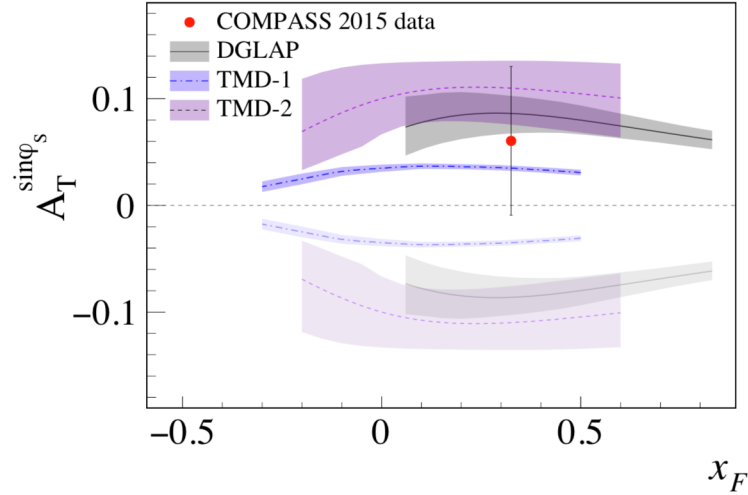


Figure 2.5: The Sivers TSA along with theory curves for the expected sign change (solid curves) and without the sign change (opaque curves). Theory curves and uncertainties are calculated using  $Q^2$  evolution from DGLAP [8], TMD-1 [9], TMD-2 [10]. This image is taken from [7].

## 2.3 Double Ratio Analysis

The double ratio method is used to determine spin-dependent asymmetry amplitudes. This means the asymmetry amplitudes  $A_T^{\sin \phi_s}$ ,  $A_T^{\sin(2\phi + \phi_s)}$  and  $A_T^{\sin(2\phi - \phi_s)}$  can be determined from the 2015 transversely polarized Drell-Yan data. The benefit of this method is that the spectrometer acceptance does not effect the determination of the asymmetry amplitudes. The author of this thesis performed the analysis in this section and found results consistent with those determined from TSA analysis.

### 2.3.1 Asymmetry Extraction

The double ratio is defined as

$$R_D(\Phi) = \frac{N_1^\uparrow(\Phi)N_2^\uparrow(\Phi)}{N_1^\downarrow(\Phi)N_2^\downarrow(\Phi)}, \quad (2.1)$$

where  $N$  represents the counts, 1(2) is the upstream(downstream) target cell and  $\uparrow(\downarrow)$  denotes the transverse polarization direction. The number of counts,  $N(\Phi)$ , is defined as

$$N(\Phi) = L * \sigma(\Phi) * a(\Phi), \quad (2.2)$$

where  $L$  is the luminosity,  $\sigma$  is the cross-section and  $a$  is the acceptance. In Eq. 2.2 the acceptance is a function of detector efficiencies and the spectrometer acceptance. When assuming the spin-dependent Drell-Yan cross-section, Eq. ??, the number of counts,  $N(\Phi)$ , can be written

$$N(\Phi) = a(\Phi)L\sigma_U \left( 1 \pm D_{[\Phi]} |S_T| A_T^w \sin(\Phi) \right). \quad (2.3)$$

where +(-) is for target polarized up(down). Therefore the double ratio can be written

$$\begin{aligned} R_D(\Phi) &= \frac{a_1^\uparrow(\Phi)L_1^\uparrow\sigma_U \left( 1 + D_{[\Phi]1}^\uparrow |S_{T1}^\uparrow| A_T^w \sin(\Phi) \right) a_2^\uparrow(\Phi)L_2^\uparrow\sigma_U \left( 1 + D_{[\Phi]2}^\uparrow |S_{T2}^\uparrow| A_T^w \sin(\Phi) \right)}{a_1^\downarrow(\Phi)L_1^\downarrow\sigma_U \left( 1 - D_{[\Phi]1}^\downarrow |S_{T1}^\downarrow| A_T^w \sin(\Phi) \right) a_2^\downarrow(\Phi)L_2^\downarrow\sigma_U \left( 1 - D_{[\Phi]2}^\downarrow |S_{T2}^\downarrow| A_T^w \sin(\Phi) \right)} \\ &= \left( \frac{a_1^\uparrow(\Phi)a_2^\uparrow(\Phi)}{a_1^\downarrow(\Phi)a_2^\downarrow(\Phi)} \right) \left( \frac{L_1^\uparrow L_2^\uparrow}{L_1^\downarrow L_2^\downarrow} \right) \frac{\left( 1 + D_{[\Phi]1}^\uparrow |S_{T1}^\uparrow| A_T^w \sin(\Phi) \right) \left( 1 + D_{[\Phi]2}^\uparrow |S_{T2}^\uparrow| A_T^w \sin(\Phi) \right)}{\left( 1 - D_{[\Phi]1}^\downarrow |S_{T1}^\downarrow| A_T^w \sin(\Phi) \right) \left( 1 - D_{[\Phi]2}^\downarrow |S_{T2}^\downarrow| A_T^w \sin(\Phi) \right)}. \end{aligned} \quad (2.4)$$

As is described in Sec 2.1.1, the data is collected in two week periods where the conditions of the spectrometer are frozen for each data taking period. For this reason the following reasonable acceptance assumption is made

$$\frac{a_1^\uparrow(\Phi)a_2^\uparrow(\Phi)}{a_1^\downarrow(\Phi)a_2^\downarrow(\Phi)} = C. \quad (2.5)$$

where  $C$  is a constant. In addition  $L_2^{\downarrow(\uparrow)} = rL_1^{\uparrow(\downarrow)}$  where  $r$  is a constant reduction factor and therefore the luminosity terms cancel out as

$$\frac{L_1^\uparrow L_2^\uparrow}{L_1^\downarrow L_2^\downarrow} = \frac{L_1^\uparrow r L_1^\downarrow}{L_1^\downarrow r L_1^\uparrow} = 1. \quad (2.6)$$

Finally the asymmetry amplitudes and target polarizations are assumed to be small so the double ratio can be simplified to

$$\begin{aligned}
R_D(\Phi) &= C \frac{\left(1 + D_{[\Phi]1}^{\uparrow} |S_{T1}^{\uparrow}| A_T^w \sin(\Phi)\right) \left(1 + D_{[\Phi]2}^{\uparrow} |S_{T2}^{\uparrow}| A_T^w \sin(\Phi)\right)}{\left(1 - D_{[\Phi]1}^{\downarrow} |S_{T1}^{\downarrow}| A_T^w \sin(\Phi)\right) \left(1 - D_{[\Phi]2}^{\downarrow} |S_{T2}^{\downarrow}| A_T^w \sin(\Phi)\right)} \\
&\approx C \frac{1 + \left[D_{[\Phi]1}^{\uparrow} |S_{T1}^{\uparrow}| + D_{[\Phi]2}^{\uparrow} |S_{T2}^{\uparrow}|\right] A_T^w \sin(\Phi)}{1 - \left[D_{[\Phi]1}^{\downarrow} |S_{T1}^{\downarrow}| + D_{[\Phi]2}^{\downarrow} |S_{T2}^{\downarrow}|\right] A_T^w \sin(\Phi)} \\
&\approx C \left(1 + \left[D_{[\Phi]1}^{\uparrow} |S_{T1}^{\uparrow}| + D_{[\Phi]2}^{\uparrow} |S_{T2}^{\uparrow}|\right] A_T^w \sin(\Phi)\right) \left(1 + \left[D_{[\Phi]1}^{\downarrow} |S_{T1}^{\downarrow}| + D_{[\Phi]2}^{\downarrow} |S_{T2}^{\downarrow}|\right] A_T^w \sin(\Phi)\right) \\
&\approx C \left(1 + \left[D_{[\Phi]1}^{\uparrow} |S_{T1}^{\uparrow}| + D_{[\Phi]2}^{\uparrow} |S_{T2}^{\uparrow}| + D_{[\Phi]1}^{\downarrow} |S_{T1}^{\downarrow}| + D_{[\Phi]2}^{\downarrow} |S_{T2}^{\downarrow}|\right] A_T^w \sin(\Phi)\right).
\end{aligned} \tag{2.7}$$

Then making the assumption that the polarizations,  $S_T$ , and depolarization factors,  $D_\Phi$  are approximately constant throughout a data period, the asymmetry amplitude of interest can be determined by fitting the double ratio with the function

$$f(\Phi) = [p0](1 + 4[p1]\sin(\Phi)), \tag{2.8}$$

where  $[p0]$  and  $[p1]$  are fit parameters and  $[p1]$  represents the asymmetry amplitude of interest. The  $[p1]$  parameter is later corrected for average polarization and depolarization factors.

The double ratio,  $R_D$ , is determined as a function of  $\Phi$  where the angle  $\Phi$  depends on which asymmetry amplitude is being determined. The assumption made in the measured counts formula, Eq. 2.3, is that all angles except the spin-dependent  $\Phi$  angle are integrated over. When this is the true, all the Drell-Yan cross-section fourier components integrate to zero except the constant term. The following table, Table 2.4, lists which  $\Phi$  angle is used to determine which spin-dependent asymmetry amplitude.

Table 2.4: Measured counts as a function of each  $\Phi$  angle

Asymmetry Amplitude	Corresponding TMD Function	$\Phi$ Angle	$\Phi$ Range (radians)
$A_T^{\sin(\phi_S)}$	Sivers	$\phi_S$	$[-\pi, \pi]$
$A_T^{\sin(2\phi - \phi_S)}$	Transversity	$2\phi - \phi_S$	$[-3\pi, 3\pi]$
$A_T^{\sin(2\phi + \phi_S)}$	Preztelosity	$2\phi + \phi_S$	$[-3\pi, 3\pi]$

The variance of the double ratio, assuming Poisson counting statistics, is

$$\sigma_{R_D}^2 = R_D^2(\Phi) \left( \frac{1}{N_1^{\uparrow}(\Phi)} + \frac{1}{N_2^{\uparrow}(\Phi)} + \frac{1}{N_1^{\downarrow}(\Phi)} + \frac{1}{N_2^{\downarrow}(\Phi)} \right). \tag{2.9}$$

### 2.3.2 Results

The results of the asymmetry amplitudes are determined in each of the nine periods and then combined as a weighted average. The asymmetries are calculated this way to minimize the effects of acceptance changes

between periods as the spectrometer was kept stable within each period but had the options for detector changes and repairs between periods. This resulting asymmetry amplitudes are determined from a weighted average as

$$A = \frac{\sum_{\text{period}} A_{\text{period}} \sigma_{\text{period}}^{-2}}{\sum_{\text{period}} \sigma_{\text{period}}^{-2}}, \quad \delta A = \sqrt{\sum_{\text{period}} \frac{1}{\sigma_{\text{period}}^{-2}}}. \quad (2.10)$$

For each period and each kinematical bin, the asymmetry is determined by fitting the double ratio and with Eq. 2.8. The results of the fit actually determines the quantity

$$A_T^w \langle D_{[\Phi]} \rangle \langle |S_T| \rangle. \quad (2.11)$$

The asymmetry amplitude is finally determined by dividing the fit results by the average polarization and depolarization values per period.

To determine the asymmetry amplitude, the double ratio is binned in eight bins in  $\Phi$ . Eight bins are chosen due to the low statistics from Drell-Yan data. Fig. 2.6 shows an example of the binned double ratio and fit results.

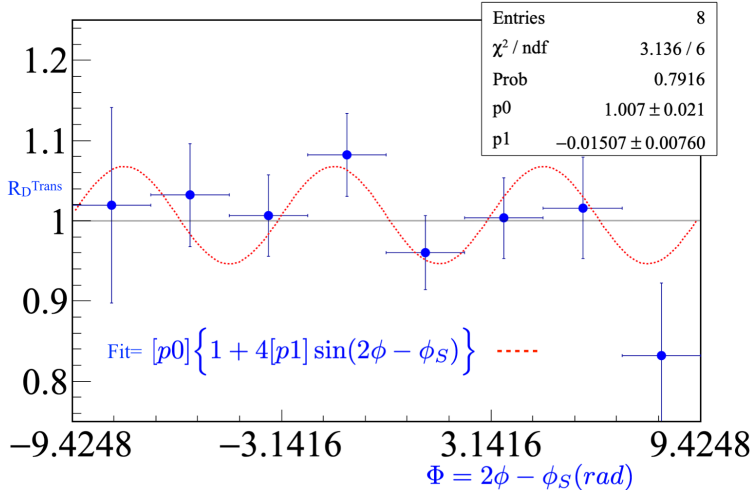


Figure 2.6: An example double ratio and corresponding fit (red) to determine the amplitude  $A_T^{\sin(2\phi - \phi_S)}$

The results for all the spin-dependent asymmetry amplitudes are shown in Fig. 2.7. As can be seen, the significance of the integrated asymmetry amplitudes is: over 1 sigma above zero for the Sivers,  $A_T^{\sin \phi_S}$ , over 3 sigma above zero for Preztelosity,  $A_T^{\sin(2\phi + \phi_S)}$ , and 3 sigma below zero for transversity,  $A_T^{\sin(2\phi - \phi_S)}$ .

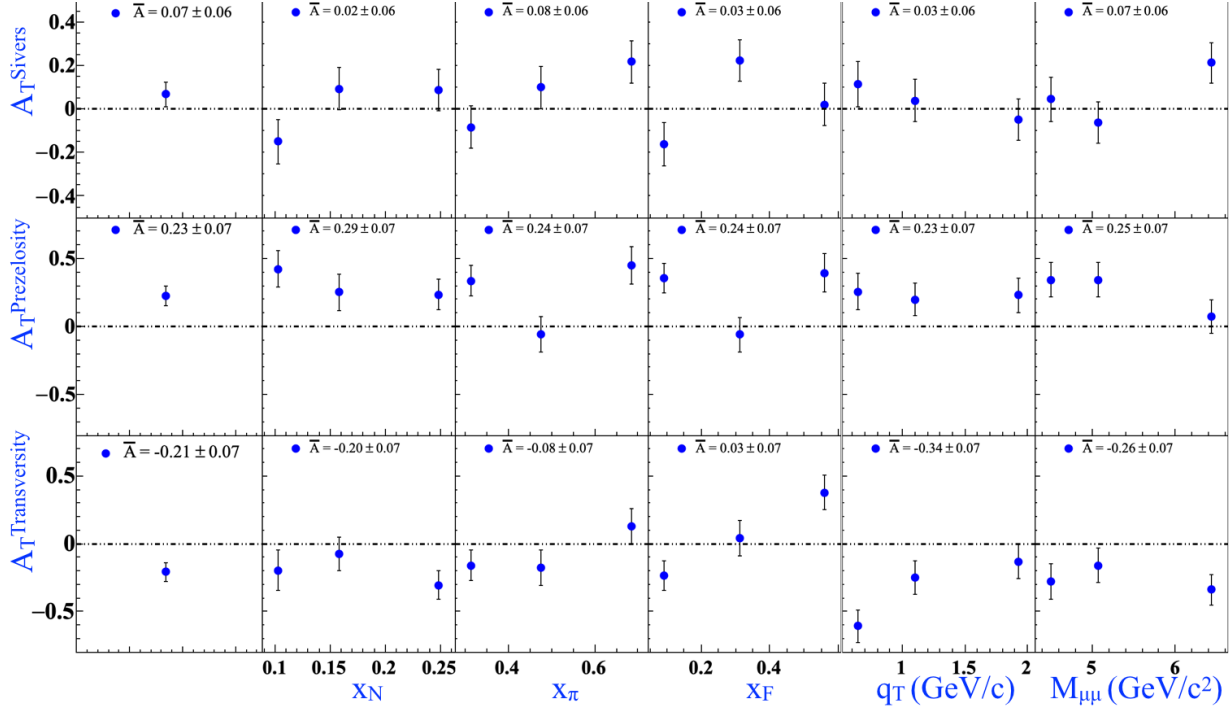


Figure 2.7: The results and statistical error bars for the transverse spin-dependent asymmetry amplitudes  $A_T^{\sin \phi_S}$  (top),  $A_T^{\sin(2\phi+\phi_S)}$  (middle) and  $A_T^{\sin(2\phi-\phi_S)}$  (bottom) determined from the double ratio method.

## 2.4 $q_T$ -Weighted Asymmetries

The  $q_T$  weighting asymmetries analysis is used to determine three asymmetry amplitudes related to TMD functions. This analysis determined the three amplitudes:  $A_T^{\sin(\phi_S)q_T/M_N}$ ,  $A_T^{\sin(2\phi+\phi_S)q_T^3/(2M_\pi M_N^2)}$  and  $A_T^{\sin(2\phi-\phi_S)q_T/M_\pi}$  which are related to the Sivers, Prezelosity and transversity TMD PDFs respectively.

The theoretical introduction and motivation for measuring  $q_T$ -weighted asymmetries is provided in Sec ???. The author of this thesis was a cross checker for the  $q_T$ -weighted asymmetry results which is a required step for any results to become public. For the full details of the  $q_T$ -weighted analysis see reference [11].

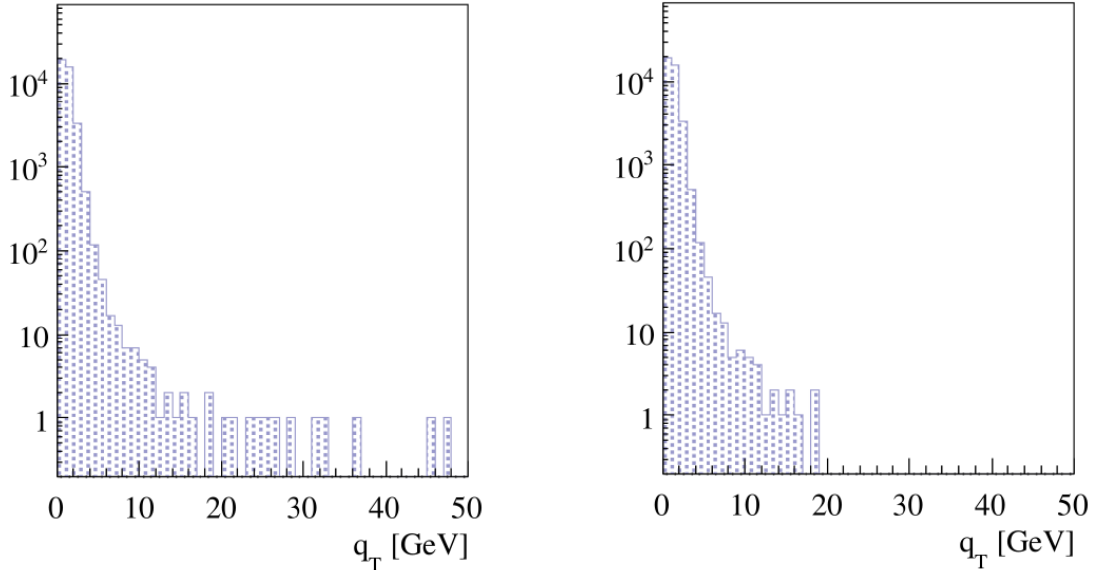
### 2.4.1 Event Selection

The results for this analysis were released prior to the slot1 reconstruction production and therefore this analysis uses the t3 reconstruction. For  $q_T$ -weighted asymmetries the results depend on the full range of the  $q_T$  distribution. In the other analyses in this chapter however, a cut was placed on high and low  $q_T$  values to ensure better azimuthal angular resolution and quality reconstructed events. This cut cannot be applied for  $q_T$ -weighted analysis because it will effect the weighting used to determine the asymmetry. On the other hand the combinatorial background and badly reconstructed events from the high  $q_T$  phase space should

be cut. The next section goes into the details and the remedy for a  $q_T$  related cut. All of the other cuts from Sec 2.1.3 are the same except for this  $q_T$  cut. Table 2.9 provides the final cut order and the remaining statistics after each cut for this  $q_T$ -weighted analysis.

### High $q_T$

The  $q_T$  distribution without any  $q_T$  cuts is shown in Fig. 2.8a. As can be seen the  $q_T$  distribution reaches values much higher than the maximum 5 GeV/c cut from the other analyses in this chapter. The most fundamental problem with this  $q_T$  distribution is that some of the events violate conservation of momentum. A first remedy to the high  $q_T$  values then is to add a cut which demands momentum conservation. This is achieved by demanding that the momentum sum of the detected muons is physically possible,  $\ell^+ + \ell^- < 190$  GeV/c. Note that this cut does not take into account the momentum spread of the beam due to the fact that the beam momentum spread is expected to be small. Fig. 2.8b shows how this cut effects the  $q_T$  distribution. As can be seen,  $q_T$  still reaches values much higher than the 5 GeV/c cut from the other TMD analyses. The remaining high  $q_T$  events still have the potential to be poorly reconstructed events or combinatorial background and for this reason an additional cut was put on the individual muons transverse momentum such that  $\ell_T^\pm < 7$  GeV/c.



(a)  $q_T$  distribution without cuts on  $q_T$ . All other cuts expect the  $q_T$  cut from table 2.1.3 are applied. This image is from [11]

(b)  $q_T$  distribution after the momentum conservation cut is added,  $\ell^+ + \ell^- < 190$  GeV/c. All other cuts expect the  $q_T$  cut from table 2.1.3 are applied. This image is from [11]

Cuts	Events	% Remaining
$\mu^+ \mu^-$ from best primary vertex, $4.3 < M_{\mu\mu} < 8.5 \text{ GeV}/c^2$	1,159,349	100.00
Triggers: (2LAS or LASxOT) and not LASxMiddle	868,291	74.89
$Z_{first} < 300 \text{ cm}, Z_{last} > 1500 \text{ cm}$	784,379	67.66
$\Delta t$ defined	776,643	66.99
$ \Delta t  < 5 \text{ ns}$	337,081	32.18
$\chi^2_{track}/\text{ndf} < 10$	370,054	31.92
$\ell^+ + \ell^- < 190 \text{ GeV}/c$	219,304	18.92
$\ell_T^\pm < 7 \text{ GeV}/c$	219,014	18.89
Trigger Validation	168,939	14.57
Good Spills	137,812	11.89
$0 < x_\pi x_N < 1, -1 < x_F < 1$	137,802	11.89
Z Vertex within NH <sub>3</sub>	42,646	3.68
Vertex Radius < 1.9cm	39,088	3.37

Figure 2.9: Event selection statistics for  $q_T$ -weighed asymmetry analysis from all periods combined

#### 2.4.2 Binning

As with the other analyses in this chapter, the asymmetry is determined in bins of the Drell-Yan physical kinematic variables:  $x_N$ ,  $x_\pi$ ,  $x_F$  and  $M_{\mu\mu}$  and an overall integrated value. No  $q_T$  binning is used however, because a full integrating of the  $q_T$  variable needs to be taken into account to form the weighted asymmetry.

#### 2.4.3 Asymmetry Method

The weighted asymmetry amplitudes  $A_T^{\sin(\phi_S)q_T/M_N}$ ,  $A_T^{\sin(2\phi+\phi_S)q_T^3/(2M_\pi M_N^2)}$  and  $A_T^{\sin(2\phi-\phi_S)q_T/M_\pi}$  are all determined using a modified double ratio. As with the double ratio method from Sec 2.3, the modified double ratio does not depend on the spectrometer acceptance. The modified double ratio is defined as

$$R_{DM}^W(\Phi) = \frac{N_1^{\uparrow W} N_2^{\uparrow W} - N_1^{\downarrow W} N_2^{\downarrow W}}{\sqrt{(N_1^{\uparrow W} N_2^{\uparrow W} + N_1^{\downarrow W} N_2^{\downarrow W})(N_1^{\uparrow} N_2^{\uparrow} + N_1^{\downarrow} N_2^{\downarrow})}}, \quad (2.12)$$

where similar notation is used from the previous analyses where  $\uparrow(\downarrow)$  is the transverse polarization direction, 1(2) denotes the upstream(downstream) cell,  $N^W$  is the weighted counts,  $W$  is the weight used and  $N$  denotes the unweighted counts. The angles  $\Phi$ , in the modified double ratio, are the same used for the double ratio, Table 2.4, and give access to asymmetry amplitudes related to the same corresponding TMD functions. Under the same reasonable acceptance ratio assumption, Eq. 2.5, from the double ratio method the acceptance cancels out in the double ratio method. Using this assumption, the modified double ratio reduces to

$$R_{DM}^W(\Phi) \approx 2\tilde{D}_{\sin\Phi}\langle S_T \rangle A_T^{\sin(\Phi)W} \sin\Phi, \quad (2.13)$$

where  $\tilde{D}_{\sin\Phi}$  is an integrated depolarization factor defined as

$$\tilde{D}_{\sin\phi_S} = 1, \quad \tilde{D}_{\sin(2\phi \pm \phi_S)} = \frac{\int a(\theta) \sin^2 \theta d\cos\theta}{\int a(\theta)(1 + \cos^2\theta)d\cos\theta} = \frac{1 - \langle \cos^2\theta \rangle}{1 + \langle \cos^2\theta \rangle}. \quad (2.14)$$

The statistical error for the modified double ratio is

$$\sigma_{R_{DM}^W}^2 = \frac{\sum_{c,p} \sigma_{N_c^{pW}}^2 4(N_1^\uparrow N_2^\uparrow) N_1^\downarrow N_2^\downarrow)^2}{\sum_{c,p} \sigma_{N_c^p}^2 (N_1^\uparrow N_2^\uparrow + N_1^\downarrow N_2^\downarrow)^4} \sum_{c,p} \frac{1}{N_c^p}, \quad (2.15)$$

where  $\sigma_{N_c^{pW}}^2 = \sum(W_c^p)^2$  is the sum of event weights,  $c$  is cell 1 or cell 2 and  $p$  is polarization  $\uparrow$  or  $\downarrow$ .

The weighted asymmetry amplitude are determined by forming the modified double ratio in eight bins in the appropriate  $\Phi$  angle and fitting this distribution. If an infinite number of bins where used and there was sufficient data, the modified double ratio would be the function form of Eq. 2.13. Due to the limited statistics however,  $R_{DM}^W$  must be binned in a finite number of bins. Therefore to account for the fact that ratio is determined in a finite number of  $\Phi$  bins, the average value of Eq. 2.13 over the bin width is used as the fit distribution. This means the functional fit is

$$\langle R_{DM}^W \rangle = \frac{1}{\Delta\Phi} \int_{\Phi_i - \frac{\Delta\Phi}{2}}^{\Phi_i + \frac{\Delta\Phi}{2}} R_{DM}^W(\Phi') d\Phi' = \frac{2}{\Delta\Phi} \sin\left(\frac{\Delta\Phi}{2}\right) R_{DM}^W(\Phi_i), \quad (2.16)$$

where  $\Delta\Phi = \frac{2\pi}{8}$  for eight bins in  $\Phi$ . Fig. 2.10 shows the double ratio as a function of  $\Phi = \phi_S$  for period W07 in one bin of  $x_N$ . One  $R_{DM}^W$  is determined for each of the 3 (number of bins)  $\times$  9 (number of periods)  $\times$  3 (number of asymmetry amplitudes) = 81 modified double ratios.

#### 2.4.4 Results

As explained in Sec 2.3.2, the asymmetry amplitudes are determine for each period and the final asymmetry is determined as a period weighted average as in Eq. 2.10. For the same reason as the previous analyses and explained in Sec 2.3.2, the polarization and depolarization factors from each period are used to correct the asymmetry amplitude determined in each period. The final results are shown in Fig. 2.11 along with the results from the release values. As can be seen the results agree with those results obtained for the release which was a requirement before the results could be release to the public.

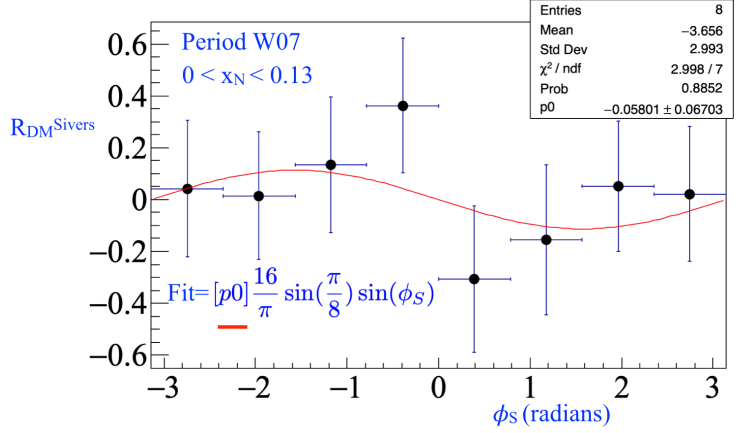


Figure 2.10: The double ratio as a function of  $\phi_S$  used to determine the Sivers asymmetry amplitude. This is for period W07 and the lowest bin in  $x_N$ . The red line shows the fit. The results of the fit are shown in the statistics box.

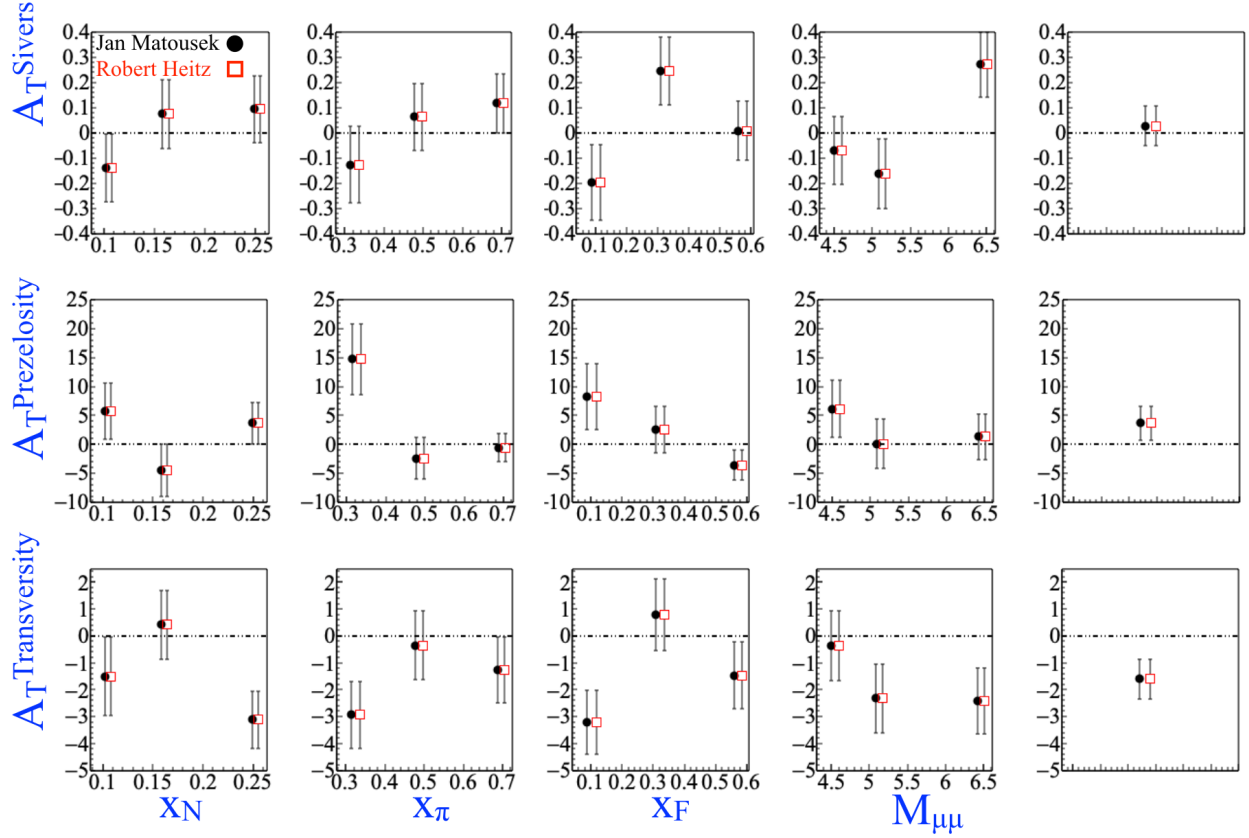


Figure 2.11: The comparison of weighted asymmetry amplitude results from the released values from Jan Matousek (black) and the cross checker Robert Heitz (red). From the top row down the asymmetry amplitudes are  $A_T^{\sin(\phi_S)q_T/M_N}$ ,  $A_T^{\sin(2\phi+\phi_S)q_T^3/(2M_\pi M_N^2)}$  and  $A_T^{\sin(2\phi-\phi_S)q_T/M_\pi}$  respectively.

## 2.5 Left-Right Asymmetries

This section goes over the analysis details for measuring the left-right asymmetry from transversely polarized Drell-Yan data. A theoretical introduction showing how the left-right asymmetry is related to TMD PDFs and related past result for this asymmetry are given in Sec ???. In short the measured asymmetry can be defined as

$$A_{lr} = \frac{\sigma_{Left} - \sigma_{Right}}{\sigma_{Left} + \sigma_{Right}}. \quad (2.17)$$

There are many ways to determine the left-right asymmetry denoted as  $A_N$ . The relevant techniques for the 2015 COMPASS setup are described and compared to ensure confidence in the end results. Sec. 2.5 starts with a general introduction to the notations and ideas used for all the asymmetry methods.

### Geometric Mean

In simple words, the number of counts detected is the number of possible chances for an event to occur times the probability for an event to occur and that the event will be detected. To get spin-dependent counts for the left-right asymmetry, the target, polarization and left or right direction relative to the spin have to be included in the counts. Generically this can be written

$$N_{cell,L(R)}^{\uparrow(\downarrow)} = \varepsilon_{cell,spectrometer\ direction}^{\uparrow(\downarrow)} * L_{cell}^{\uparrow(\downarrow)} * \sigma_{L(R)}, \quad (2.18)$$

where  $\uparrow$  ( $\downarrow$ ) denotes the target polarization, cell is either cell 1 for the upstream target cell or cell 2 for the downstream target cell,  $L(R)$  is left(right) of the spin direction and spectrometer direction denotes either the spectrometer Jura side or the Saleve side corresponding to where the event was detected.

The most basic method to determine  $A_N$  per target cell is

$$A_N = \frac{1}{P} \frac{N_L - N_R}{N_L + N_R}, \quad (2.19)$$

where the counts,  $N$ , are defined as Eq. ??, and  $P$  denotes the fraction of polarized nucleons. An intuitive picture of left and right defined in the target frame is shown in Fig. 2.12.

The previous definitions of the detected counts, Eq. 2.18 and Eq. ??, and therefore also Eq. 2.19 all depend on the spectrometer acceptance. This is a problem because the spectrometer acceptance can change with time and space and therefore can be dependent on the physical kinematics which produced the event. Such dependencies can cause unphysical false asymmetries in the measurement of  $A_N$  and must therefore be removed or must be included as systematic effects.

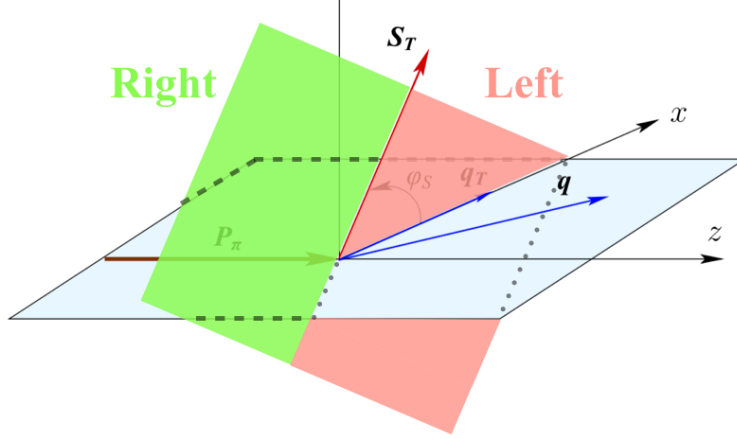


Figure 2.12: The definition of the left plane (red) and right plane (green) defined from a target spin up configuration in the target frame

Forming the geometric mean asymmetry is, however, a way to determine the left-right asymmetry without acceptance effects from the spectrometer. It is defined as

$$\frac{1}{P} \frac{\sqrt{N_{\text{cell } 1(2),L}^{\uparrow} N_{\text{cell } 1(2),L}^{\downarrow}} - \sqrt{N_{\text{cell } 1(2),R}^{\uparrow} N_{\text{cell } 1(2),R}^{\downarrow}}}{\sqrt{N_{\text{cell } 1(2),L}^{\uparrow} N_{\text{cell } 1(2),L}^{\downarrow}} + \sqrt{N_{\text{cell } 1(2),R}^{\uparrow} N_{\text{cell } 1(2),R}^{\downarrow}}}, \quad (2.20)$$

where  $P$  represents the fraction of polarized nucleons. Table ?? summarizes the notations used throughout this chapter.

Table 2.5: Notations used in defining the left/right asymmetry

Notation	Description
L(R)	virtual photon detected left(right) of spin
Jura(Saleve)	spectrometer west(east) side
cell 1(2)	up(down)stream target cell
$\uparrow$ ( $\downarrow$ )	target cell polarized up(down)
P	fraction of polarized target nucleons

Equation 2.20 can be thought of simply as the normalized difference of left minus right counts. Left and right counts are determined relative to the target spin directions and are defined as

$$\begin{aligned} \text{Left} : \hat{q}_T \cdot (\hat{S}_T \times \hat{P}_\pi) &> 0 \\ \text{Right} : \hat{q}_T \cdot (\hat{S}_T \times \hat{P}_\pi) &< 0, \end{aligned} \quad (2.21)$$

where  $\hat{q}_T$ ,  $\hat{S}_T$  and  $\hat{P}_\pi$  are unit vectors in the target reference frame for the virtual photon transverse momentum, the target spin and the beam pion momentum respectively.

Using Eq. 2.18 for the definition of counts, the geometric mean asymmetry is

$$\frac{1}{P} \frac{\kappa_{\text{geomean}} \sqrt{\sigma_L \sigma_L} - \sqrt{\sigma_R \sigma_R}}{\kappa_{\text{geomean}} \sqrt{\sigma_L \sigma_L} + \sqrt{\sigma_R \sigma_R}}, \quad (2.22)$$

where  $\kappa$  is a ratio of acceptances defined as

$$\kappa_{\text{geomean}} = \frac{\sqrt{a_{\text{cell 1(2),Jura}}^{\uparrow} a_{\text{cell 1(2),Saleve}}^{\downarrow}}}{\sqrt{a_{\text{cell 1(2),Saleve}}^{\uparrow} a_{\text{cell 1(2),Jura}}^{\downarrow}}}. \quad (2.23)$$

Here the detection side of spectrometer is specified by looking down the beam line as either Jura to mean left or Saleve to mean right. These relations of Jura is left and Saleve is right are only strictly true if the target polarization is pointing straight up in the target frame. In particular if the beam particle and the target polarization do not make a right angle in the laboratory frame this relation will no longer be strictly true but is an approximation for ease of notation.

Relation 2.22 is equal to  $A_N$  if  $\kappa$  is equal to one. However as stated previously, time effects can vary  $\kappa$  from unity. These effects are estimated through false asymmetry analysis and included in the systematic error bars described in section 2.5.1. Equation 2.20 is therefore to a good approximation an acceptance free method to determine  $A_N$ . It is also defined for the upstream and downstream cells independently and therefore can be used as a consistency check between the two target cells.

The statistical uncertainty of the geometry mean is

$$\frac{1}{P} \frac{\sqrt{N_L^{\uparrow} N_L^{\downarrow} N_R^{\uparrow} N_R^{\downarrow}}}{\left(\sqrt{N_L^{\uparrow} N_L^{\downarrow}} + \sqrt{N_R^{\uparrow} N_R^{\downarrow}}\right)^2} \sqrt{\frac{1}{N_L^{\uparrow}} + \frac{1}{N_L^{\downarrow}} + \frac{1}{N_R^{\uparrow}} + \frac{1}{N_R^{\downarrow}}}, \quad (2.24)$$

which reduces to  $\frac{1}{P} \frac{1}{\sqrt{N}}$  in the case of equal statistics in each direction from each target cell polarization.

## Two-Target Geometric Mean

As described in section 2.1 COMPASS had two oppositely polarized target cells in 2015. The previous geometric mean asymmetry, however, determined an  $A_N$  per target. It is desirable from a statistical point of view, however, to determine one  $A_N$  from the 2015 COMPASS setup. It is also desirable for comparison purposes to determine  $A_N$  using all the information from the 2015 COMPASS setup. This can be accomplished by modifying the geometric mean to add both target cells as follows

$$\frac{1}{P} \frac{\sqrt[4]{N_{\text{cell } 1,\text{L}}^{\uparrow} N_{\text{cell } 1,\text{L}}^{\downarrow} N_{\text{cell } 2,\text{L}}^{\uparrow} N_{\text{cell } 2,\text{L}}^{\downarrow}} - \sqrt[4]{N_{\text{cell } 1,\text{R}}^{\uparrow} N_{\text{cell } 1,\text{R}}^{\downarrow} N_{\text{cell } 2,\text{R}}^{\uparrow} N_{\text{cell } 2,\text{R}}^{\downarrow}}}{\sqrt[4]{N_{\text{cell } 1,\text{L}}^{\uparrow} N_{\text{cell } 1,\text{L}}^{\downarrow} N_{\text{cell } 2,\text{L}}^{\uparrow} N_{\text{cell } 2,\text{L}}^{\downarrow}} + \sqrt[4]{N_{\text{cell } 1,\text{R}}^{\uparrow} N_{\text{cell } 1,\text{R}}^{\downarrow} N_{\text{cell } 2,\text{R}}^{\uparrow} N_{\text{cell } 2,\text{R}}^{\downarrow}}}. \quad (2.25)$$

As in the basic geometric mean asymmetry, section 2.5, left and right are determined relative to the spin direction of the target as in Eq. 2.21. Again using Eq. 2.18 for the definition of counts, the two target geometric mean asymmetry, Eq. 2.25, can be written as

$$\frac{1}{P} \frac{\kappa_{\text{two-target}} \sqrt[4]{\sigma_L \sigma_L \sigma_L \sigma_L} - \sqrt[4]{\sigma_R \sigma_R \sigma_R \sigma_R}}{\kappa_{\text{two-target}} \sqrt[4]{\sigma_L \sigma_L \sigma_L \sigma_L} + \sqrt[4]{\sigma_R \sigma_R \sigma_R \sigma_R}}, \quad (2.26)$$

,

where now  $\kappa_{\text{two-target}}$  is the ratio of acceptances from all targets and polarizations. This inclusive acceptance ratio is defined as

$$\kappa_{\text{two-target}} = \frac{\sqrt[4]{a_{\text{cell } 1,\text{Jura}}^{\uparrow} a_{\text{cell } 1,\text{Saleve}}^{\downarrow} a_{\text{cell } 2,\text{Jura}}^{\uparrow} a_{\text{cell } 2,\text{Saleve}}^{\downarrow}}}{\sqrt[4]{a_{\text{cell } 1,\text{Saleve}}^{\uparrow} a_{\text{cell } 1,\text{Jura}}^{\downarrow} a_{\text{cell } 2,\text{Saleve}}^{\uparrow} a_{\text{cell } 2,\text{Jura}}^{\downarrow}}}. \quad (2.27)$$

In this case the acceptance ratio is expected to vary less with time and therefore be closer to unity than the normal geometric mean acceptance ratio, Eq. 2.23. This is a consequence of having the different target cells oppositely polarized. Rewriting Eq. 2.27 with sub-period superscripts instead of target polarization superscripts

$$\kappa_{\text{two-target}} = \frac{\sqrt[4]{a_{\text{cell } 1,\text{Jura}}^a a_{\text{cell } 1,\text{Saleve}}^b a_{\text{cell } 2,\text{Jura}}^b a_{\text{cell } 2,\text{Saleve}}^a}}{\sqrt[4]{a_{\text{cell } 1,\text{Saleve}}^a a_{\text{cell } 1,\text{Jura}}^b a_{\text{cell } 2,\text{Saleve}}^b a_{\text{cell } 2,\text{Jura}}^a}}, \quad (2.28)$$

where sub-period  $a$  is with the upstream target polarized up and the downstream target polarized down and vice versa for sub-period  $b$ . From Eq. 2.28 it is more evident that the acceptance ratio terms for sub-period  $b$  are reciprocal to the terms for sub-period  $a$  and therefore the acceptance ratio is expected to be more stably close to unity.

Finally the statistical uncertainty of the two target geometric mean is

$$\frac{1}{P} \frac{LR}{(L+R)^2} \sqrt{\sum_{\text{cell polarization}} \left( \frac{1}{N_{\text{cell},\text{L}}^{\text{polarization}}} + \frac{1}{N_{\text{cell},\text{R}}^{\text{polarization}}} \right)}, \quad (2.29)$$

where L can be thought of as the left counts and equals to  $\sqrt[4]{N_{\text{cell } 1,\text{L}}^{\uparrow} N_{\text{cell } 1,\text{L}}^{\downarrow} N_{\text{cell } 2,\text{L}}^{\uparrow} N_{\text{cell } 2,\text{L}}^{\downarrow}}$  and R can be thought of as the right counts and equals  $\sqrt[4]{N_{\text{cell } 1,\text{R}}^{\uparrow} N_{\text{cell } 1,\text{R}}^{\downarrow} N_{\text{cell } 2,\text{R}}^{\uparrow} N_{\text{cell } 2,\text{R}}^{\downarrow}}$ . The statistical uncertainty for the two target geometric mean also reduces to  $\frac{1}{P} \frac{1}{\sqrt{N}}$  in the case of equal statistic populations in each

direction and target polarization.

### 2.5.1 Systematic Studies

Several tests were performed to estimate the systematic uncertainty of the left-right asymmetry. The systematic errors are determined by adding all non-zero systematic uncertainties in quadrature. The impact from each source of systematic error is summarized in Tab. 2.8.

#### Period Compatibility (Time Dependence)

The asymmetries calculated for each time period in each kinematic bin are shown in Fig. 2.13.

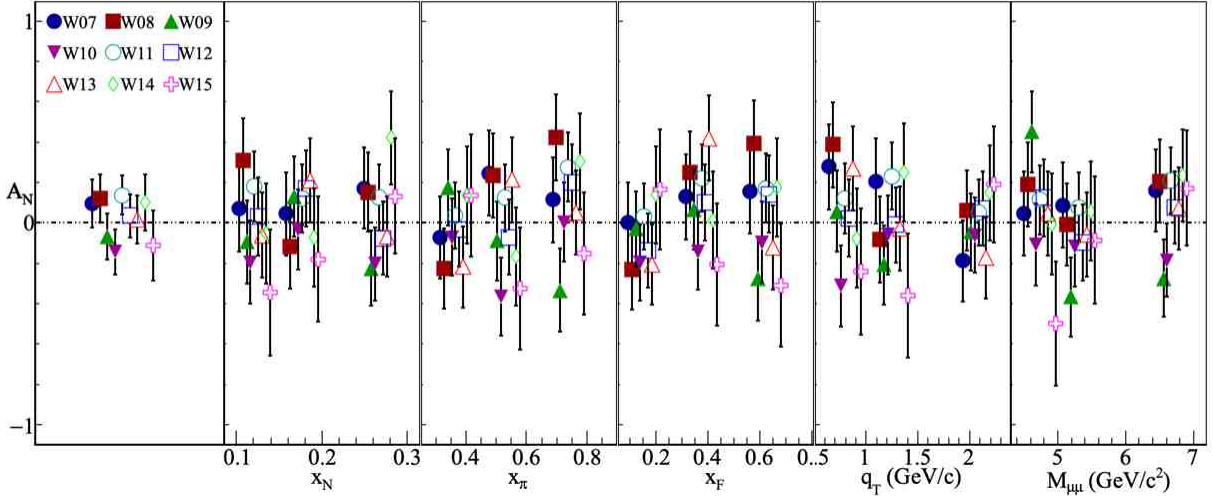


Figure 2.13:  $A_N$  determined for each period

By eye the asymmetry fluctuations appear to be statistically compatible. To quantify the compatibility of the asymmetries between the periods, a pull distribution is formed. The pull value is defined as

$$\Delta A_i = \frac{A_i - \langle A \rangle}{\sqrt{\sigma_{A_i}^2 - \sigma_{\langle A \rangle}^2}}, \quad (2.30)$$

and is determined for each period and kinematic bin. There are therefore 3 (number of bins)  $\times$  5 (number of kinematics)  $\times$  9 (number of periods) = 135 entries in the pull distribution. This distribution is shown in Fig. 2.14 along with a Gaussian fit. If the asymmetries all come from the same parent distribution then due to the central limit theorem the pull distribution will be a Gaussian distribution with zero mean and unit variance. The discrepancy of the pull distribution from a standard Gaussian distribution is used to

determine a systematic error as

$$\frac{\sigma_{\text{systematic}}}{\sigma_{\text{statistical}}} = \sqrt{|\sigma_{\text{pull}}^2 - 1|} + \frac{\mu_{\text{pull}}}{2}. \quad (2.31)$$

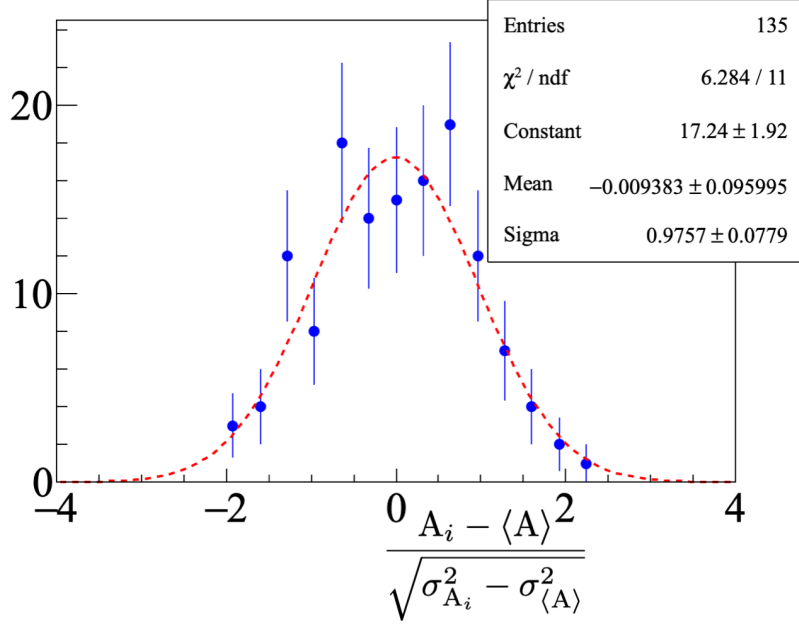


Figure 2.14: Pull distribution from the two target geometric mean

As the asymmetries in different kinematic bins are formed using the same data set the asymmetries between kinematic binning are correlated. For this reason an uncorrelated pull distribution is also formed for each kinematic bin and also compared with a standard Gaussian distribution. These distributions are shown in Fig. 2.15 and the results of the Gaussian fit are shown in Fig. 2.16. For these uncorrelated pull distributions there are now only 3 (number of bins) x 9(number of periods) = 27 entries in each kinetically binned pull distributions and only 9 (number of periods) bins in the integrated pull distribution.

Even though the Gaussian fits did not give exactly a standard Gaussian, the fit parameters are well compatible with a standard Gaussian within the errors of the fit. Therefore no systematic error was assigned due to incompatibility of the periods.

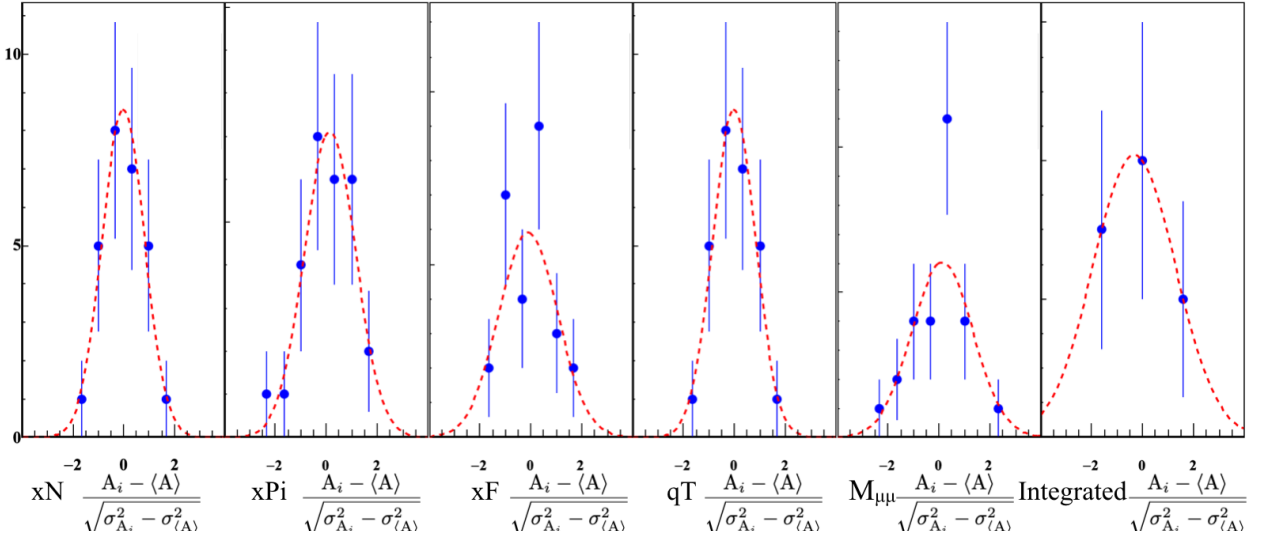


Figure 2.15: Uncorrelated pull distributions

Entries	27	Entries	27	Entries	27	Entries	27	Entries	27	Entries	9
$\chi^2 / \text{ndf}$	0.4347 / 3	$\chi^2 / \text{ndf}$	1.056 / 4	$\chi^2 / \text{ndf}$	3.416 / 3	$\chi^2 / \text{ndf}$	0.4347 / 3	$\chi^2 / \text{ndf}$	3.152 / 4	$\chi^2 / \text{ndf}$	1.091e-08 / 0
Constant	$8.548 \pm 2.043$	Constant	$7.101 \pm 1.827$	Constant	$5.922 \pm 1.622$	Constant	$8.548 \pm 2.043$	Constant	$6.038 \pm 1.603$	Constant	$4.085 \pm 1.992$
Mean	$-0.01562 \pm 0.17221$	Mean	$0.1422 \pm 0.2204$	Mean	$-0.1036 \pm 0.2910$	Mean	$-0.01562 \pm 0.17221$	Mean	$0.1287 \pm 0.2860$	Mean	$-0.3308 \pm 0.8192$
Sigma	$0.8386 \pm 0.1304$	Sigma	$1.004 \pm 0.201$	Sigma	$1.15 \pm 0.31$	Sigma	$0.8386 \pm 0.1304$	Sigma	$1.197 \pm 0.256$	Sigma	$1.616 \pm 1.101$

Figure 2.16: Results of Gaussian fit for the uncorrelated pull distributions

### False Asymmetries

#### Acceptance From False Asymmetries

As was pointed out in Sec. 2.5 and Sec. 2.5, the asymmetry measurement assumes the acceptance does not change with time and therefore the acceptance ratios Eq. 2.23 and Eq. 2.27 are unitary. Any deviation from a unitary acceptance ratio is estimated with a false asymmetry and is taken as a systematic error. To determine if acceptance does change with time, a false asymmetry is calculated where the only way the false

asymmetry could be non-zero if acceptance changes with time. This false asymmetry for the two target geometric mean is

$$A_{N,\text{False}} = \frac{1}{P} \frac{\sqrt[4]{N_{\text{cell } 1,R}^{\uparrow} N_{\text{cell } 1,L}^{\downarrow} N_{\text{cell } 2,L}^{\uparrow} N_{\text{cell } 2,R}^{\downarrow}} - \sqrt[4]{N_{\text{cell } 1,L}^{\uparrow} N_{\text{cell } 1,R}^{\downarrow} N_{\text{cell } 2,R}^{\uparrow} N_{\text{cell } 2,L}^{\downarrow}}}{\sqrt[4]{N_{\text{cell } 1,R}^{\uparrow} N_{\text{cell } 1,L}^{\downarrow} N_{\text{cell } 2,L}^{\uparrow} N_{\text{cell } 2,R}^{\downarrow}} + \sqrt[4]{N_{\text{cell } 1,L}^{\uparrow} N_{\text{cell } 1,R}^{\downarrow} N_{\text{cell } 2,R}^{\uparrow} N_{\text{cell } 2,L}^{\downarrow}}} \quad (2.32)$$

$$= \frac{1}{P} \frac{\alpha \sqrt[4]{\sigma_R \sigma_L \sigma_L \sigma_R} - \sqrt[4]{\sigma_L \sigma_R \sigma_R \sigma_L}}{\alpha \sqrt[4]{\sigma_R \sigma_L \sigma_L \sigma_R} + \sqrt[4]{\sigma_L \sigma_R \sigma_R \sigma_L}}$$

$$= \frac{1}{P} \frac{\alpha - 1}{\alpha + 1}, \quad (2.33)$$

where  $\alpha$  is an acceptance ratio and is defined as

$$\alpha = \frac{\sqrt[4]{a_{\text{cell } 1,\text{Saleve}}^{\uparrow} a_{\text{cell } 1,\text{Saleve}}^{\downarrow} a_{\text{cell } 2,\text{Jura}}^{\uparrow} a_{\text{cell } 2,\text{Jura}}^{\downarrow}}}{\sqrt[4]{a_{\text{cell } 1,\text{Jura}}^{\uparrow} a_{\text{cell } 1,\text{Jura}}^{\downarrow} a_{\text{cell } 2,\text{Saleve}}^{\uparrow} a_{\text{cell } 2,\text{Saleve}}^{\downarrow}}}. \quad (2.34)$$

The false asymmetry, Eq. 2.32, can be simplified as

$$A_{N,\text{False}} = \frac{1}{P} \frac{\sqrt[4]{N_{\text{cell } 1,\text{Saleve}} N_{\text{cell } 2,\text{Jura}}} - \sqrt[4]{N_{\text{cell } 1,\text{Jura}} N_{\text{cell } 2,\text{Saleve}}}}{\sqrt[4]{N_{\text{cell } 1,\text{Saleve}} N_{\text{cell } 2,\text{Jura}}} + \sqrt[4]{N_{\text{cell } 1,\text{Jura}} N_{\text{cell } 2,\text{Saleve}}}}. \quad (2.35)$$

That is  $A_{N,\text{false}}$  is the normalized difference of counts from each target cell assuming the upstream target is always polarized down and the downstream target is always polarized up. Given that the polarization flips for both upstream and downstream target cells,  $A_{N,\text{false}}$  is an asymmetry where physical effects cancel out. The kinematic dependencies of the false asymmetry are shown in Fig. 2.17 and the kinematic dependencies of the acceptance ratio,  $\alpha$ , are shown in Fig. 2.18.

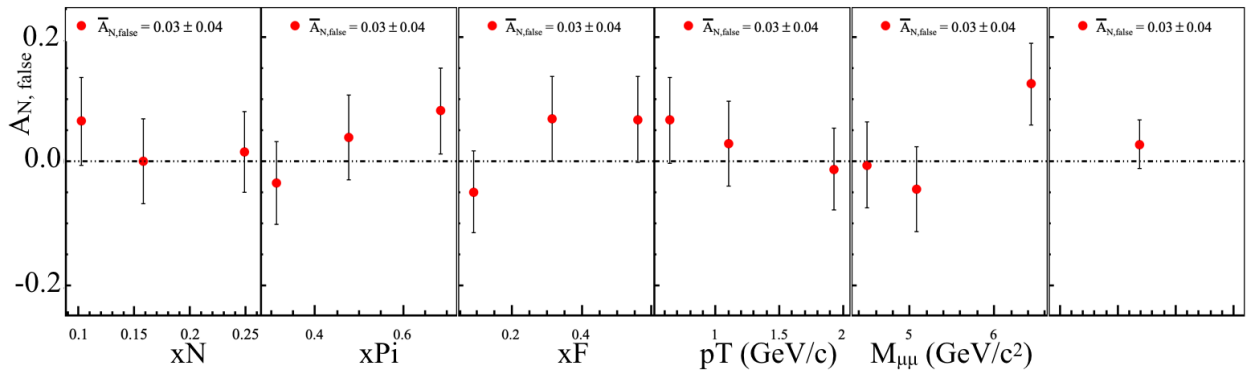


Figure 2.17: False asymmetry to estimate fluctuations in acceptance in time

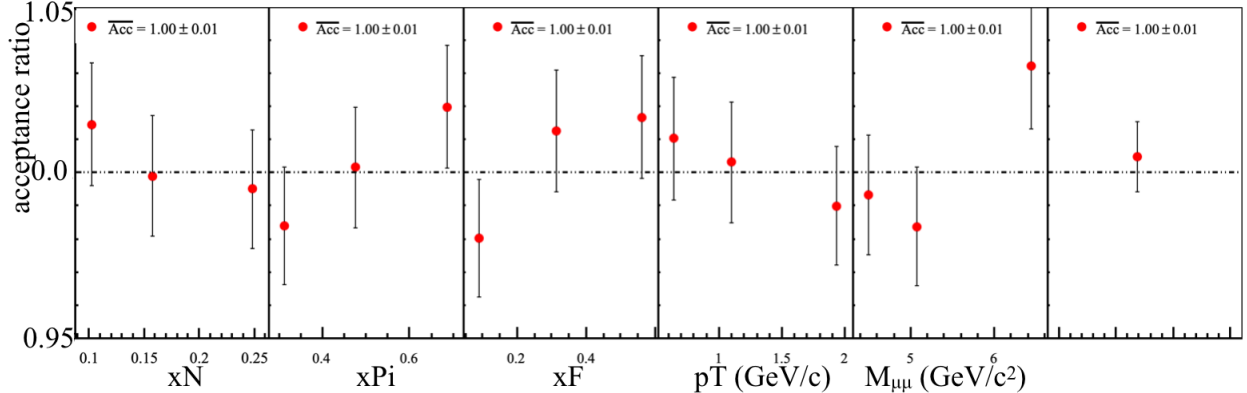


Figure 2.18: Acceptance ratio, Eq. 2.34, used to determine the systematic effects from acceptance changes in time

While  $\alpha$  is an acceptance ratio it is not the same as the acceptance ratio in the true asymmetry. However  $\alpha$  is similar to the true acceptance ratio,  $\kappa$ , in that  $\alpha$  will only be different from unity as a result of time changes in the spectrometer. Therefore it is assumed  $\alpha$  can be used as a good estimate of the true acceptance ratio fluctuations. The systematic error due to acceptance fluctuations is determined as

$$\delta A_{N,\text{systematic}} = \frac{1}{P} \left( \frac{|\alpha - 1|}{2} + \delta_{\frac{|\alpha-1|}{2}} \right), \quad (2.36)$$

where this expression is derived in Appendix ???. The kinematic dependence of the systematic error normalized to the statistical error is shown in Fig. 2.19. The binned average systematic error due to acceptance is 20% of the statistical error.

### Further False Asymmetry Effects

Although the list of systematic effects specifically studied is quite exhaustive there is always the potential for other systematic effects not considered. Studies of the changes in time from additional false asymmetries were performed in an attempt to take into account all other systematic effects. All false asymmetries considered must be constructed in such a way that the physical process of interest cancels out. A false asymmetry could therefore only be non-zero from acceptance effects, luminosity or some other reason not considered. The additional false asymmetries are constructed in a way that luminosity effects cancel out and acceptance effects are approximately constant. With these assumptions, the pull values from Eq. 2.30 are expected to be distributed as a standard Gaussian distribution. Any deviation from a standard Gaussian is conservatively taken as a systematic effect from some unknown cause. The additional studied false

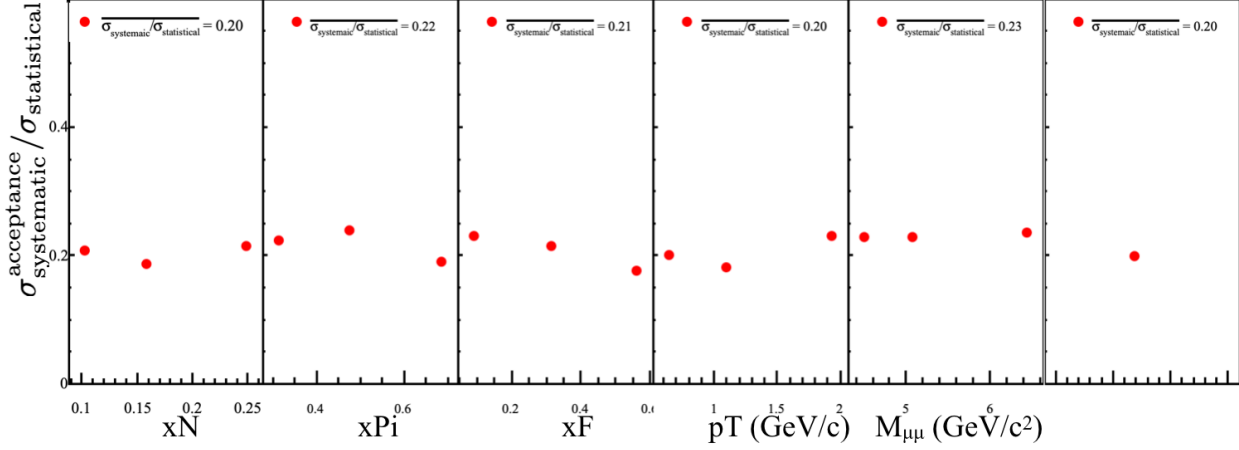


Figure 2.19: Systematic error due to acceptance effects

asymmetries are summarized in the following enumerated list.

1. A false asymmetry similar to Eq. 2.32 but with the upstream left and right counts flipped defined as

$$\frac{1}{P} \frac{\sqrt[4]{N_{\text{cell } 1,L}^{\uparrow} N_{\text{cell } 1,R}^{\downarrow} N_{\text{cell } 2,L}^{\uparrow} N_{\text{cell } 2,R}^{\downarrow}} - \sqrt[4]{N_{\text{cell } 1,R}^{\uparrow} N_{\text{cell } 1,L}^{\downarrow} N_{\text{cell } 2,R}^{\uparrow} N_{\text{cell } 2,L}^{\downarrow}}}{\sqrt[4]{N_{\text{cell } 1,L}^{\uparrow} N_{\text{cell } 1,R}^{\downarrow} N_{\text{cell } 2,L}^{\uparrow} N_{\text{cell } 2,R}^{\downarrow}} + \sqrt[4]{N_{\text{cell } 1,R}^{\uparrow} N_{\text{cell } 1,L}^{\downarrow} N_{\text{cell } 2,R}^{\uparrow} N_{\text{cell } 2,L}^{\downarrow}}}. \quad (2.37)$$

This false asymmetry can be thought of as measuring the normalized counts on the Jura side minus the Saleve side. The period weighted average results of this false asymmetry are shown in Fig. 2.20 and as can be seen there is the asymmetry is systematically less than zero by more than a standard deviation. The uncorrelated pull distributions from this false asymmetry are shown in Fig. 2.21 and the corresponding Gaussian fit results are shown in Fig. 2.22. Due to the fact that there are less entries in these pull distributions the Gaussian fit results are not necessarily that good. In an attempt to correct for this and to take into account the fit errors, a weighted average of the mean and standard deviation are made, as in Eq. 2.10, using weights as the inverse fit variances. The resulting systematic error is again determined as in Eq. 2.31 using the weighted mean and weighted standard deviation.

2. A false asymmetries using only the information from the upstream or the downstream target defined as

$$\frac{1}{P} \frac{\sqrt{N_{\text{cell } 1(2),L}^{\uparrow} N_{\text{cell } 1(2),R}^{\downarrow}} - \sqrt{N_{\text{cell } 1(2),R}^{\uparrow} N_{\text{cell } 1(2),L}^{\downarrow}}}{\sqrt{N_{\text{cell } 1(2),L}^{\uparrow} N_{\text{cell } 1(2),R}^{\downarrow}} + \sqrt{N_{\text{cell } 1(2),R}^{\uparrow} N_{\text{cell } 1(2),L}^{\downarrow}}}. \quad (2.38)$$

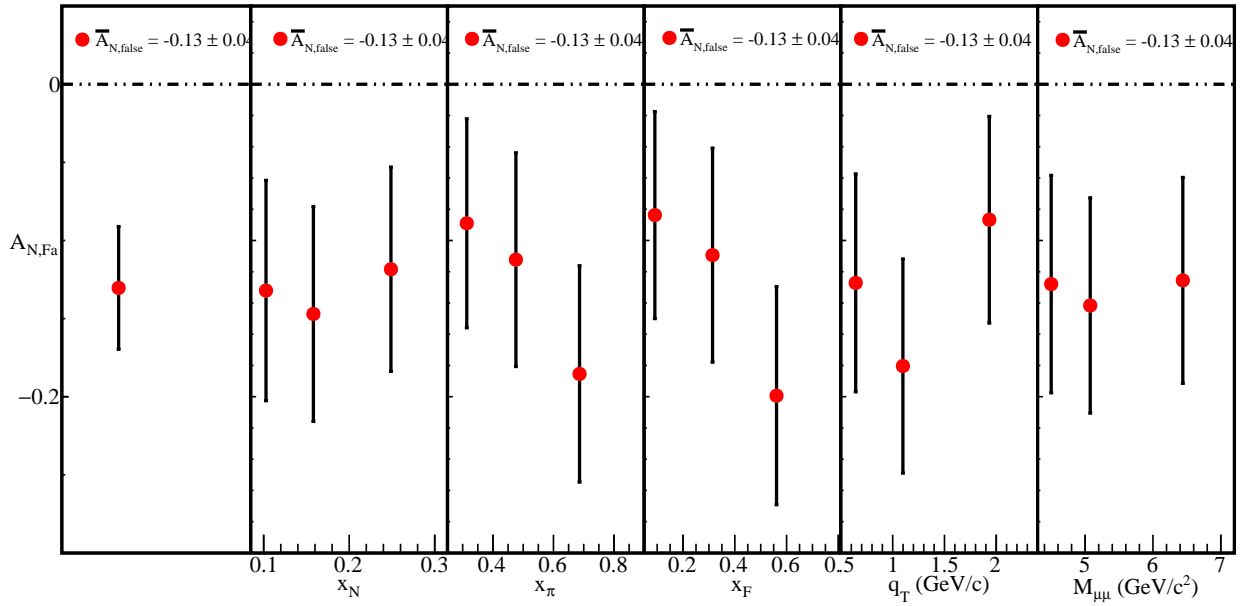


Figure 2.20: Two target geomean false asymmetry. This is non-zero due to acceptance effects

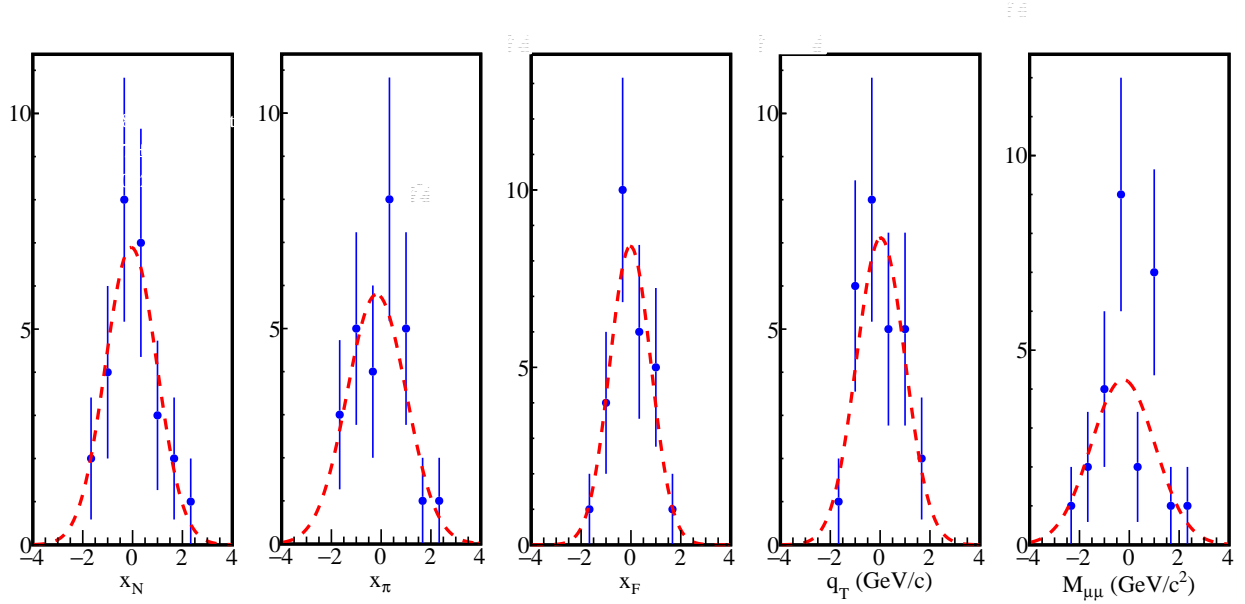


Figure 2.21: Uncorrelated pulls of the two target geomean false asymmetry

This false asymmetry can also be thought of as measuring the normalized counts on the Jura side minus the Saleve side but for each target individually. Both this false asymmetry and the previous false asymmetry can be written as Eq. 2.33 where  $\alpha$  will be an acceptance ratio of Jura/Saleve. As the Jura/Saleve acceptance ratio is expected to be the same for the upstream and downstream

Entries	27	Entries	27	Entries	27	Entries	27	Entries	27
$\chi^2 / \text{ndf}$	1.06 / 4	$\chi^2 / \text{ndf}$	2.875 / 4	$\chi^2 / \text{ndf}$	1.203 / 3	$\chi^2 / \text{ndf}$	1.925 / 3	$\chi^2 / \text{ndf}$	7.364 / 5
Constant	$6.898 \pm 2.019$	Constant	$5.797 \pm 1.578$	Constant	$8.419 \pm 2.089$	Constant	$7.116 \pm 1.826$	Constant	$4.248 \pm 1.307$
Mean	$-0.05617 \pm 0.22189$	Mean	$-0.1796 \pm 0.3545$	Mean	$-0.02243 \pm 0.17361$	Mean	$0.0256 \pm 0.2382$	Mean	$-0.2528 \pm 0.3265$
Sigma	$1.032 \pm 0.266$	Sigma	$1.187 \pm 0.317$	Sigma	$0.8256 \pm 0.1377$	Sigma	$0.9721 \pm 0.1962$	Sigma	$1.279 \pm 0.331$

Figure 2.22: Gaussian fit results for the uncorrelated two target false geomean pulls

targets, any difference between the two false asymmetries must be due to other reasons. A by period comparison between the upstream and downstream target is shown in Fig. 2.23 and as can be seen there are differences by period between the upstream and downstream asymmetries. A combined pull distribution is made using the information from both upstream and downstream asymmetries and is shown in Fig. 2.24. As with the previous false asymmetry, lack of data leads to the same problems with fit and therefore the same weighting method is used to determine a systematic error.

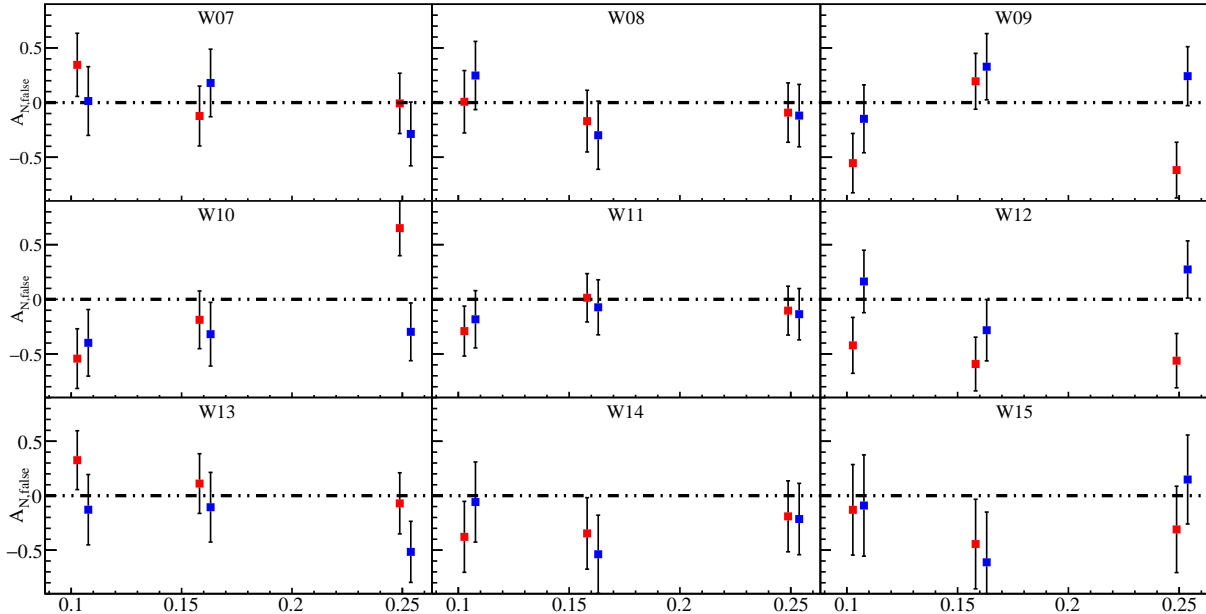


Figure 2.23: One target false asymmetries for the upstream target (red) and the downstream target (blue), as a function of  $x_N$ . Each graph is from a different period in time.

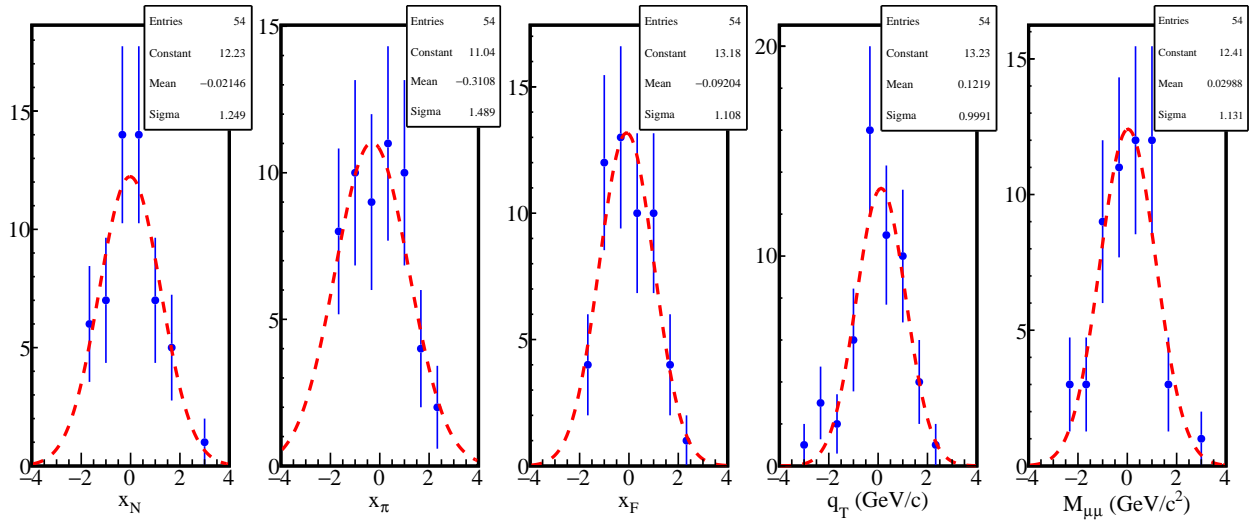


Figure 2.24: Pull values from one target geomean false asymmetries. Both upstream and downstream values are used to make this pull

- Finally the same false asymmetry used to determine the acceptance fluctuations, Eq. 2.32, is also checked for compatibility and a systematic error is determined in the same way as the previous false asymmetries. The pulls are shown in Fig. 2.25 and the corresponding fit parameters are shown in Fig. 2.26.

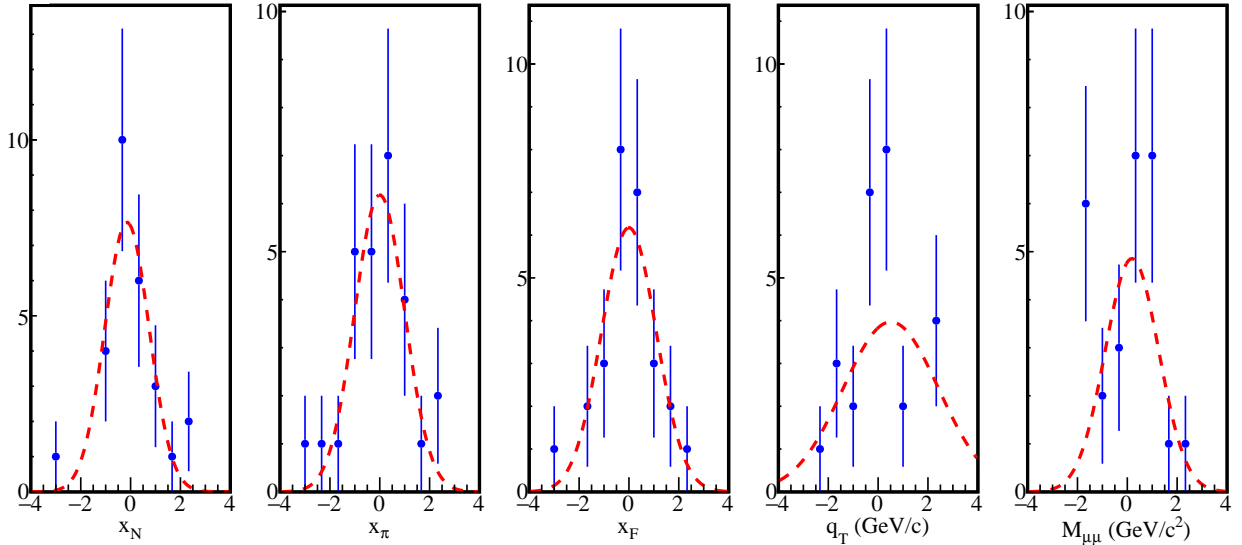


Figure 2.25: Pull distribution for a nearly acceptance free two target false geomean asymmetry

A summary of the systematic error from each false asymmetry is shown in Tab. 2.6

Entries	27	Entries	27	Entries	27	Entries	27	Entries	27
$\chi^2 / \text{ndf}$	3.517 / 4	$\chi^2 / \text{ndf}$	3.737 / 6	$\chi^2 / \text{ndf}$	2.357 / 5	$\chi^2 / \text{ndf}$	6.734 / 4	$\chi^2 / \text{ndf}$	7.973 / 4
Constant	$7.658 \pm 3.014$	Constant	$6.183 \pm 1.859$	Constant	$6.176 \pm 2.115$	Constant	$3.971 \pm 1.201$	Constant	$4.857 \pm 4.667$
Mean	$-0.1441 \pm 0.2765$	Mean	$-0.002351 \pm 0.211941$	Mean	$-0.002406 \pm 0.246275$	Mean	$0.5095 \pm 1.1086$	Mean	$0.1882 \pm 0.9446$
Sigma	$0.891 \pm 0.424$	Sigma	$1.004 \pm 0.226$	Sigma	$1.098 \pm 0.361$	Sigma	$1.92 \pm 1.12$	Sigma	$1.072 \pm 1.195$

Figure 2.26: Gaussian fit results for the previous pull distributions

Systematic error	$\langle \sigma_{\text{systematic}} / \sigma_{\text{statistical}} \rangle$
Two target Jura-Saleve	0.26
Combined one target	0.5
Two target acceptance estimation	0.29

Table 2.6: Summary of systematic error impacts from false asymmetries. The maximum systematic error is chosen as the systematic error.

### Left/Right Event Migration

The spectrometer has finite resolution for any measured quantity and for this reason events measured as left outgoing could really be events that are right outgoing and vice versa for measured left outgoing events. This left-right miss-identification has the result of diluting spin-dependent effects by effectively having a sample from an unpolarized target along with the sample from the polarized target. Therefore the asymmetry  $A_N$  reduces from left-right miss-identification and this effect is included as a systematic effect.

For this thesis five Monte-Carlo processes were generated corresponding to three background processes and a spin-independent signal process. The generator used was PHTHYIA8 and the data was generated and reconstruction at Blue Waters. The background processes simulated were JPsi production, Psi' production and open charm (OC) production. Each of these backgrounds can decay into two muons which results in a background contamination to the Drell-Yan signal. Table ?? gives the parameters used for the Monte-Carlo studied.

Miss-identification was estimated from the simulated Monte-Carlo data sample described in Table ?? where the sample was made from the respond of the COMPASS spectrometer to input Drell-Yan events in a similar mass range. The same analysis performed on real data was performed on this Monte-Carlo data to

Table 2.7: Monte-Carlo settings produced on Blue Waters

Event generator	PYTHIA8
Pion pdf	GRVPI1
Proton pdf	NNPDF23
proton/neutron mixing ratio	1.96
Initial state radiation	on
Final state radiation	on
Multiple parton interactions	on
Simulated detector efficiencies	uniform

get the angles of interest. Fig. 2.27 shows the rate of events identified correctly and incorrectly as a function of the  $\phi_S$ . This plot is made by determining which outgoing direction the generated events emerged with the outgoing direction the reconstructed events emerged.

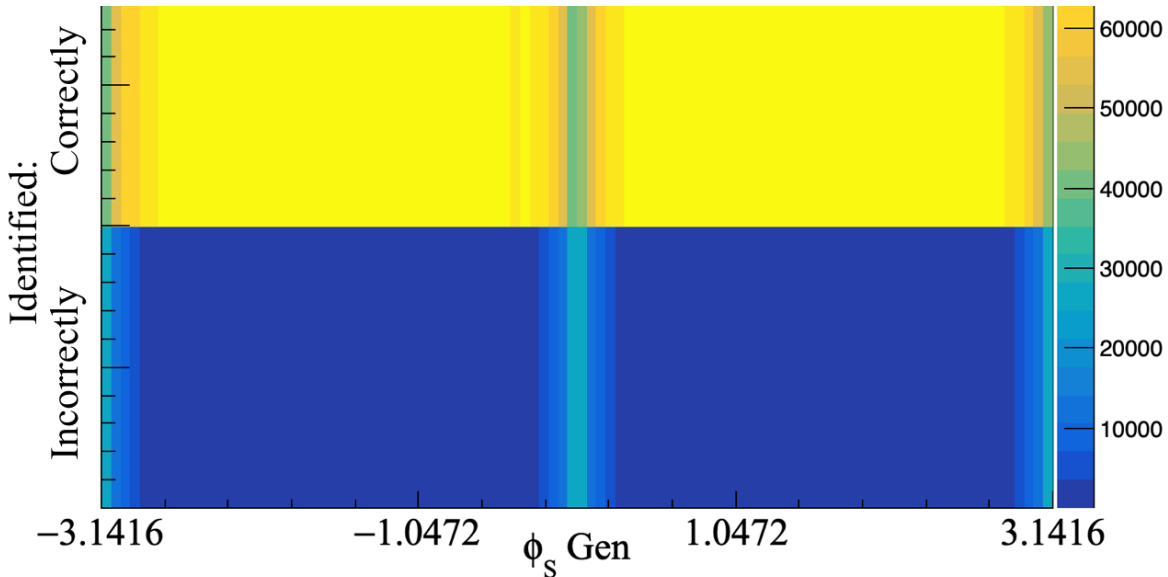


Figure 2.27: The rate of identified correctly and incorrectly left-right events as a function of  $\phi_S$ . This is determined by comparing the generated outgoing direction with the reconstructed outgoing direction. The left-right boundary is clearly visible at  $\phi_S = 0^\circ$  and  $\phi_S = -\pi^\circ$  and  $\phi_S = \pi^\circ$

As is clearly visible there is a band of higher miss-identification rate at the border between left and right. For this reason a cut in the  $\phi_S$  variable symmetric about the left-right border was tested to determine the percent of miss-identification as a function of the amount of  $\phi_S$  cut. These results are shown in Fig. 2.28.

The systematic error for left-right migration is calculated as

$$\delta A_{N,\text{systematic}} = \gamma * A_N + \gamma * \delta A_N, \quad (2.39)$$

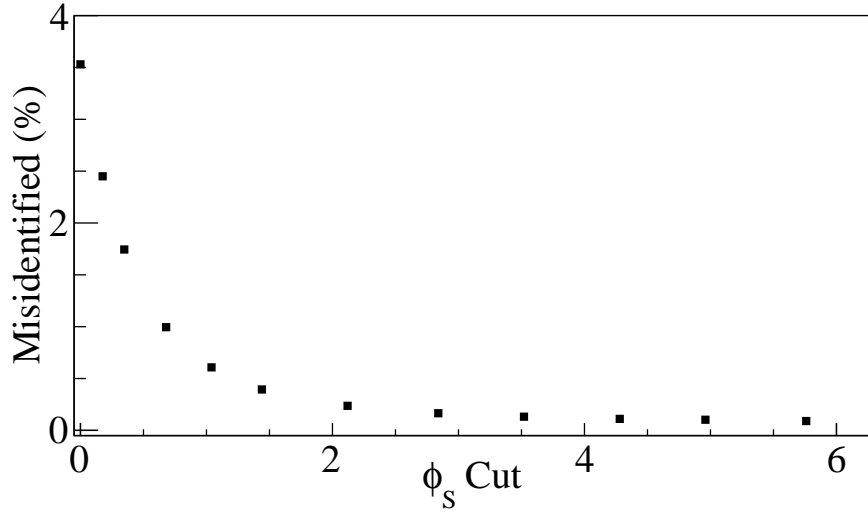


Figure 2.28: Percent left-right migration as a function of the amount of  $\phi_S$  cut.

where this expression is derived in Appendix ??.

No cut on  $\phi_S$  was used for the asymmetry due to the fact that the systematic error is already small with no cut in  $\phi_S$  and to avoid loss of statistics. The integrated systematic error due to left-right event migration was determined to be 9%.

### Total Systematics

The total systematic error is determined by adding all non-zero systematic effects in quadrature as

$$\left\langle \frac{\sigma_{\text{systematics}}}{\sigma_{\text{statistical}}} \right\rangle = \sqrt{\sum_i^{\text{all systematics}} \left\langle \frac{\sigma_{\text{systematics},i}^2}{\sigma_{\text{statistical}}^2} \right\rangle}, \quad (2.40)$$

where all the systematic effects considered are summarized in Tab. 2.8.

Systematic error	$\langle \sigma_{\text{systematic}}/\sigma_{\text{statistical}} \rangle$	$\langle \sigma_{\text{systematic}} \rangle$	$\langle \sigma_{\text{statistical}} \rangle$
Period compatibility	0.0	0.0	0.039
Acceptance fluctuation	0.2	0.008	0.039
False asymmetry	0.5	0.020	0.039
Left-Right migration	0.09	0.004	0.039
Total	0.55	0.021	0.039

Table 2.8: Summary of systematic error impacts to the integrated asymmetry

Need to include target polarization( 5%) and dilution ( 8%)

## 2.5.2 Results

(need to explain way polarization is corrected by period) weighed as 2.10

The results for the basic geometric mean are shown in Fig. 2.29 and the results for the two target geometric mean are shown in Fig. 2.30. The numerical values for the two-target geometric mean with statistical and systematic error bars are summarized in Table ???. The systematic error bars are discussed in Sec. 2.5.1.

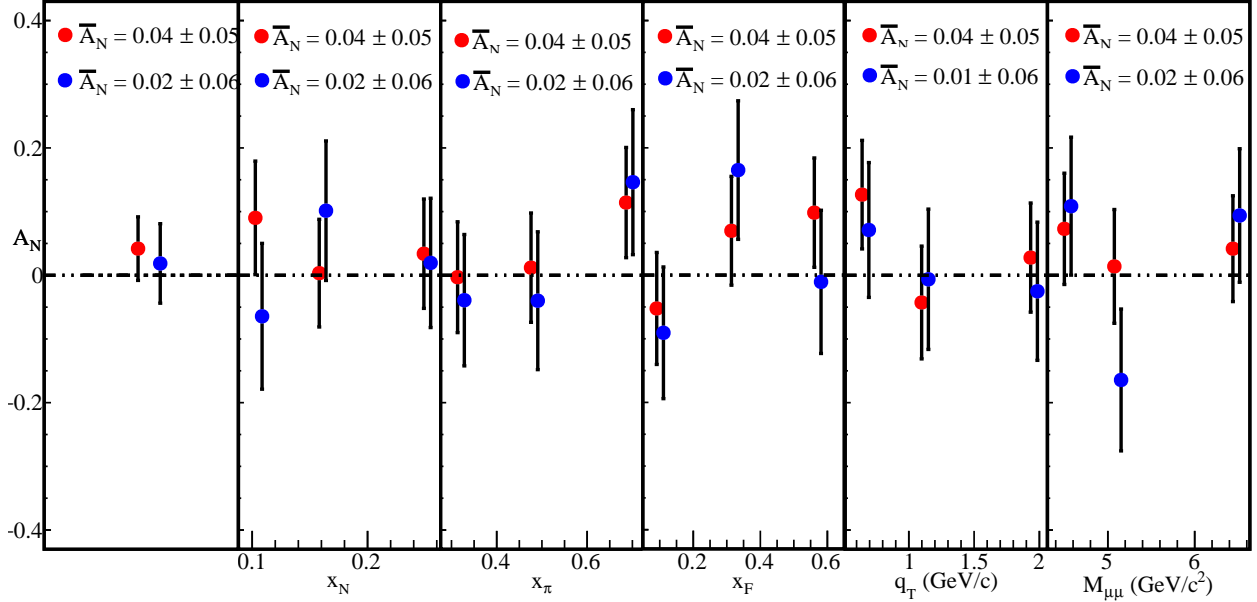


Figure 2.29:  $A_N$  determined from the geometric mean method for the upstream target (red) and the downstream target (blue) for all kinematic binnings

Table 2.9: Two-Target geometric mean numerical values and error bars for each kinematic bin

Binning variable	Bin Range	$A_N$	$\delta A_N^{\text{stat}}$	$\delta A_N^{\text{sys}}$
$\langle x_N \rangle$				

## 2.5.3 Comparison of results

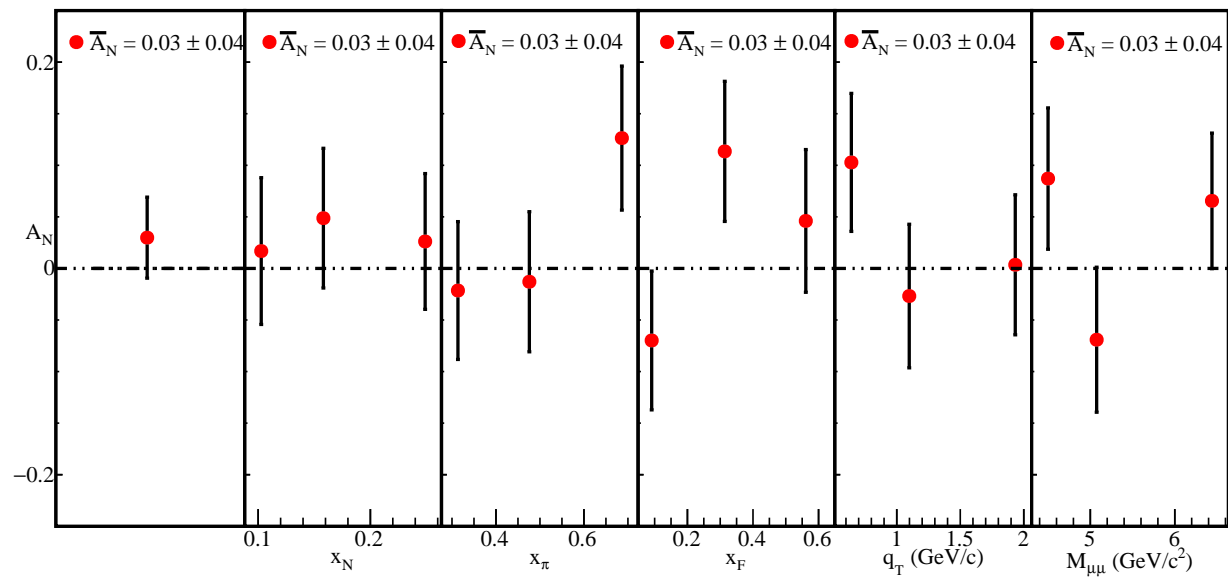


Figure 2.30:  $A_N$  determined by the two-target geometric mean method for all kinematic binnings

# References

- [1] P. Abbon et al. The COMPASS experiment at CERN. *Nucl. Instrum. Meth.*, A577:455–518, 2007. doi: 10.1016/j.nima.2007.03.026.
- [2] A. Abragam and M. Goldman. Principles of dynamic nuclear polarisation. *Reports on Progress in Physics*, 41:395–467, 1978. doi: 10.1103/PhysRevD.16.2219.
- [3] Radja Boughezal, John M. Campbell, R. Keith Ellis, Christfried Focke, Walter Giele, Xiaohui Liu, Frank Petriello, and Ciaran Williams. Color singlet production at NNLO in MCFM. *Eur. Phys. J.*, C77(1):7, 2017. doi: 10.1140/epjc/s10052-016-4558-y.
- [4] V. Yu. Aleksakhin, Y. Bedfer, S. Gerasimov, and A. Yu. Korzenev. Geometrical event reconstruction in the COMPASS experiment. *Phys. Part. Nucl. Lett.*, 4:350–362, 2007. doi: 10.1134/S1547477107040103. [Pisma Fiz. Elem. Chast. Atom. Yadra2007,no.4,588(2007)].
- [5] R. Fruhwirth. Application of Kalman filtering to track and vertex fitting. *Nucl. Instrum. Meth.*, A262: 444–450, 1987. doi: 10.1016/0168-9002(87)90887-4.
- [6] Torbjrn Sjstrand, Stefan Ask, Jesper R. Christiansen, Richard Corke, Nishita Desai, Philip Ilten, Stephen Mrenna, Stefan Prestel, Christine O. Rasmussen, and Peter Z. Skands. An Introduction to PYTHIA 8.2. *Comput. Phys. Commun.*, 191:159–177, 2015. doi: 10.1016/j.cpc.2015.01.024.
- [7] M. Aghasyan et al. First measurement of transverse-spin-dependent azimuthal asymmetries in the Drell-Yan process. *Phys. Rev. Lett.*, 119(11):112002, 2017. doi: 10.1103/PhysRevLett.119.112002.
- [8] M. Anselmino, M. Boglione, U. D’Alesio, F. Murgia, and A. Prokudin. Study of the sign change of the Sivers function from STAR Collaboration W/Z production data. *JHEP*, 04:046, 2017. doi: 10.1007/JHEP04(2017)046.
- [9] Miguel G. Echevarria, Ahmad Idilbi, Zhong-Bo Kang, and Ivan Vitev. QCD Evolution of the Sivers Asymmetry. *Phys. Rev.*, D89:074013, 2014. doi: 10.1103/PhysRevD.89.074013.
- [10] Peng Sun and Feng Yuan. Transverse momentum dependent evolution: Matching semi-inclusive deep inelastic scattering processes to Drell-Yan and W/Z boson production. *Phys. Rev.*, D88(11):114012, 2013. doi: 10.1103/PhysRevD.88.114012.
- [11] Jan Matousek. *Nucleon spin structure studies in Drell-Yan process at COMPASS*. PhD thesis, University of Trieste, April 2018.